CHALMERS

Modelling of Lower Hybrid Current Drive in the Tore Supra Tokamak

Thesis for the Degree of Master of Science

EMELIE NILSSON

Department of Applied Physics
Chalmers University of Technology
Gothenburg, Sweden 2012

Abstract

In the Tore Supra tokamak, lower hybrid (LH) waves at a frequency of 3.7 GHz are coupled to the plasma for current drive using a Full Active Multijunction (FAM) launcher and/or a Passive Active Multijunction (PAM) launcher, which was installed recently to test an ITER-relevant antenna design. A number of discharges have been performed in Tore Supra, using either or both launchers, in a variety of plasma conditions including fully non-inductive scenarios.

As a mediator between experimental measurements and current drive theory, simulations play an important role. In this work, a comparative modelling of non-inductive LH current drive with FAM and PAM launchers is presented. A suite of codes specifically coupled and optimized for LH current drive modelling is used, including a code for equilibrium and transport (METIS), LH coupling (ALOHA), LH wave propagation (C3PO), absorption (LUKE), and fast electron bremsstrahlung (FEB) emission reconstruction (R5X2). The modelling suite provides a calculation of the current profile, LH power deposition, and a synthetic diagnostic for the FEB emission of the LH accelerated electrons in the energy range $50 - 110\,\mathrm{keV}$. The reconstructed emission can be directly compared to FEB measurement from hard x-ray (HXR) detection system.

A study of fully non-inductive discharges with either the FAM or PAM launchers shows a good agreement between experiments and simulations for such discharges at relatively low density ($\bar{n} < 2 \times 10^{19}$ m^{-3}). On Tore Supra, the FAM or PAM parallel refractive index spectra ($n_\parallel$) are found to be noticeably different. In particular, a secondary lobe located at a relatively low value of $|n_\parallel|$ in the PAM has a negative contribution to the plasma current.

Radial profiles of FEB emission in the energy range $60 - 80\,\mathrm{keV}$ have routinely been used in Tore Supra analysis. The work of this thesis shows that this profile is not a valid approximation, since the HXR detectors registers a strictly positive quantity, regardless of the direction of the emitting electrons. Thus, inverted HXR profiles can be used as a relative measurement of the current profile only in the absence of secondary lobes driving a significant current. Another conclusion is that FEB emission measurement is insufficient to compare experiments that used FAM or PAM launcher in similar plasma conditions since the FEB profiles may look similar while the driven current can be very different.

Acknowledgements

I would like to express my gratitude to Tünde Fülöp, who introduced me to the world of fusion physics and inspired me with her dedication to research. Deepest gratitude to my supervisor Annika Ekedahl not only for her invaluable guidance and expertise in the lower hybrid current drive physics, but also for supporting me in the French paperwork jungle. My greatest appreciation to the enthusiastic supervision from Joan Decker, for encouragement, sharp ideas and advice. I am impressed by this young physicist who has so much energy and creativity and happy that this work is only the beginning of our collaboration.

Finally, a special mention goes out to my dear Café Borren and X-treme team girls for making me feel at home at Chalmers.

Emelie Nilsson, Aix-en-Provence June 1st, 2012

Contents

1

Introduction

The increasing global energy demands driven by population growth and rising standards of living is becoming a burning issue. The main energy sources of today are finite and give rise to greenhouse effect and pollution. To satisfy the energy needs of a growing global population, sustainable energy production with much lower environmental impact than conventional technologies must be found.

Controlled nuclear fusion has some very valuable properties as an energy source. It can be made inherently safe and fuel resources are well accessible all over the planet. With no direct contribution to the greenhouse effect and absence of waste that would burden future generations, fusion energy is an attractive candidate for delivering clean, reliable and virtually inexhaustible energy.

Though still a somewhat exotic topic on earth, nuclear fusion is the main energy source of our universe. In the sun and all other stars of the universe, hydrogen and helium nuclei are continually fusing and releasing enormous amounts of energy. Confined by strong gravitational pressure, the sun is a gigantic fusion reactor that sustains our existence on earth. By combining light nuclei into heavier elements, energy is released because of the difference in binding energy for different nuclei, according to Einstein's famous formula $E = mc^2$. The goal in fusion energy research is to recreate this process in a reactor on earth. The reaction between the hydrogen isotopes deuterium and tritium is currently considered to be most suitable for energy production because its cross section peaks at lower temperatures than for other fusion reactions.

In fission, nuclei are split by fast neutrons that are not affected by the electrical Coulomb force. Therefore a neutron can easily penetrate the nucleus. In fusion reactions *charged* nuclei have to be brought very close to each other to enable the reaction. For the fuel in a reactor to overcome the Coulomb potential barrier and fuse, the nuclei have to collide at very high speeds. This means that the temperature of the fuel has to be very high, on the order of 100 million degrees. At these temperatures, which are even higher than in the sun, the nuclei of the fuel are completely stripped from the electrons.

This state is called a *plasma* and is a mix of positively charged ions and free electrons.

The aim is to create a so called *burning plasma*, in which the heating power released in fusion reactions keeps the plasma hot so that no external heating is necessary, like in a star. A fireplace is a chemical example of ignition. One uses a match to get the fuel hot and once the burning of the wood releases heat faster than the air can carry it away the fire ignites and keeps burning. In a fusion reactor, one wants to be able to heat up the fuel once, and then let it burn without much external power being needed. Unfortunately, current fusion experiments are like wet wood fires: to keep the reaction going, external heat must constantly be added.

At this point we have succeeded in achieving fusion reactions, but it has proven difficult to confine the fuel well enough at high temperature for a practical source of electrical power. Fusion research is therefore focused on confining heat inside the plasma so that the reactor can ignite. Recreating the fusion process on earth is a great scientific and technical challenge. Mastering the complex technology of a tokamak fusion reactor has an amazing reward: clean, safe and accessible energy that can meet the energy needs of a growing population.

1.1 Nuclear fusion

Nuclear fusion is the process where atomic nuclei merge into heavier elements. This mechanism is the foundation of the enormous power of the sun and other stars, where fusion of protons into deuterium is the first step in a chain of exothermic reactions. The mass of the product is smaller than the combined mass of the fusing nuclei and the mass difference is released as energy.

There are several candidates for fusion reactions in a reactor. The reaction between the hydrogen isotopes deuterium (^{2}H) and tritium (^{3}H) has by far the largest cross-section at the lowest energies, see Figure 1.1. This makes the D-T fusion process

$$\mathrm{D} + \mathrm{T} \rightarrow {}^4\mathrm{He} + \mathrm{n} + 17.6\,\mathrm{MeV} \tag{1.1}$$

the most promising candidate for an energy-producing system.

To be a candidate for an energy-producing system, the fusion fuel has to be sufficiently abundant. Deuterium occurs naturally with a weight fraction of 3.3×10^{-5} in water. Given the water of the oceans, the static energy range is very large. Tritium is an unstable radioactive isotope. It decays to a ^{3}He ion

$$\mathrm{T} \rightarrow {}^3\mathrm{He} + e^- + \nu_e, \tag{1.2}$$

with a half-life of 12.3 years. Owing to the unstable character, no significant amounts of tritium exist in nature, but it can be produced with nuclear reactions of the neutrons from the D-T reaction and lithium.

$$\mathrm{n} + {}^6\mathrm{Li} \rightarrow {}^4\mathrm{He} + \mathrm{T} + 4.8\,\mathrm{MeV}, \tag{1.3}$$

$$\mathrm{n} + {}^7\mathrm{Li} \rightarrow {}^4\mathrm{He} + \mathrm{T} + \mathrm{n} - 2.5\,\mathrm{MeV}. \tag{1.4}$$

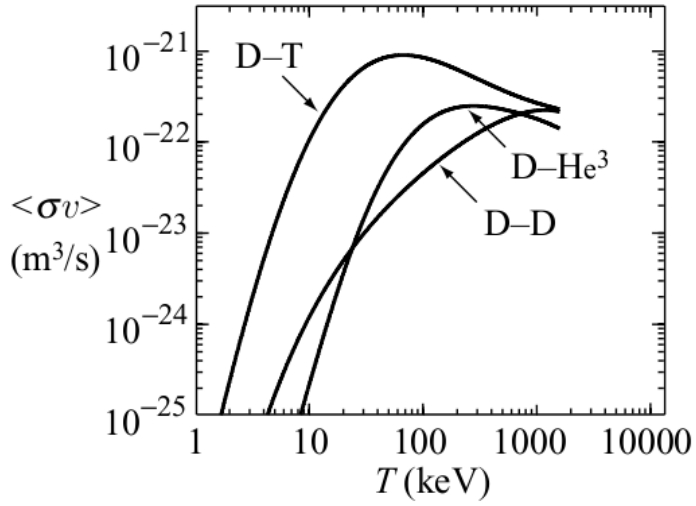

Figure 1.1: The velocity averaged cross section of fusion reactions as a function of temperature, obtained numerically from equal temperature Maxwell distributions. The D-T reaction has a maximum reaction cross section. Figure from [1].

Nuclei repel each other due to their positive charge. In order to fuse, they must be brought very close to each other, to a range on the order of 10^{-15} meters, where the attractive nuclear force is strong enough to overcome the electrostatic potential barrier. In the center of a star the enormous gravitational pressure provides the nuclei with enough energy to overcome the Coulomb repulsion and fuse. On earth other confinement methods must be used to keep the fuel in plasma state long enough for a significant part of it to fuse. A fusion process can be self sustained if the product of density, temperature and confinement time, the so called *triple product*, exceeds a certain value.

1.2 Controlled fusion in tokamaks

Charged particles can be confined by strong magnetic fields. In a cylindrical plasma the particles are confined perpendicularly to the field lines but they can escape parallel to them. By bending the cylinder into a ring shaped device end losses can be eliminated. The two main magnetic confinement fusion (MCF) reactor concepts are the *tokamak* and the *stellarator*. Both devices confine the plasma in a torus shaped magnetic cage. The main difference is that in a stellarator the magnetic field is completely created by complex shaped external coils, whereas the tokamak is axisymmetric and the poloidal magnetic field component is generated by a strong electric current flowing in the plasma.

1.2.1 Plasma confinement

Since any material would melt in contact with the extremely hot fuel, the plasma must be prevented from touching the walls of the confinement chamber. The most prominent

solution is MCF where strong magnetic fields traps the plasma. This confinement method is based on the constrained motion of the charged particles of the plasma by a magnetic field. A charged particle can move freely along magnetic field lines, but its movement perpendicular to the field lines is restricted due to the Lorentz force ($\mathbf{F} = q\mathbf{v} \times \mathbf{B}$, where q is the charge of the particle, $\mathbf{v}$ the particle velocity and $\mathbf{B}$ the magnetic field) acting on charged particles like the positively charged nuclei and negatively charged electrons that form the plasma. The Lorentz force guides the particles to move perpendicularly to the magnetic field into a circular motion around a magnetic field line resulting in gyrating particle orbits.

The curvature of the toroidal field introduces forces on the plasma that cause particle drifts and eventually disruption of the plasma. The particles tend to drift away from the magnetic flux surfaces due to mechanisms arising from the electromagnetic fields. One of them, the so called *gradient B drift*, is caused by the radial gradient in the magnetic field due to the compression of the field lines on the inside of the torus. For a charged particle the gyration radius varies with the magnetic field strength, resulting in a minimum on the high field side (the inner side of the torus) and a maximum on the low field side (the outside). This causes the particle to drift in the vertical direction. Because the ions and the electrons gyrate anti-parallel to each other they also have different drift directions, creating a charge separation with an associated electrical field.

The other drift mechanism, the so called *curvature drift*, is a result of the curvature of the field lines. As a charged particle moves along a curved magnetic field line it experiences a centrifugal force due to the field curvature that results in a drift perpendicular to both the centrifugal force and the magnetic field. Since the electrons and the ions have opposite signs of their charge, the Lorentz force will act in opposite directions. In order for a charged particle to follow a curved field line and provide the necessary centripetal force, it needs a drift velocity out of the plane of curvature.

This field accelerates and slows down the gyrating particles on the upward and downward part of their orbit, resulting, again, in longer or shorter gyration radii and an outward drift of the particle, known as $\mathbf{E} \times \mathbf{B}$ drift. This effect is the same for ions and electrons since the sign of the charge cancels out. Hence, this drift can lead to a macroscopic movement of the plasma.

To counteract the drift effect, the magnetic field is given a poloidal component by driving a current in the plasma. The magnetic field lines then follow a helical path around the torus, thus cancelling the vertical drifts. A stable plasma equilibrium can be reached by twisting the magnetic field lines by superimposing toroidal and poloidal field components. Magnetic field lines wrap around the torus axis in a helix and constrain the path of the charged particles in the fuel. In a tokamak the toroidal component is generated by poloidal magnetic coils that are wound around the torus. Figure 1.2 shows a schematic view of the tokamak concept.

The poloidal field is more complex to produce since the toroidal current must flow inside the plasma. A straightforward way to create a poloidal magnetic field is by using the plasma as a secondary circuit in a transformer, with poloidal coils surrounding the plasma. In this setup the plasma acts as a single secondary loop generating the

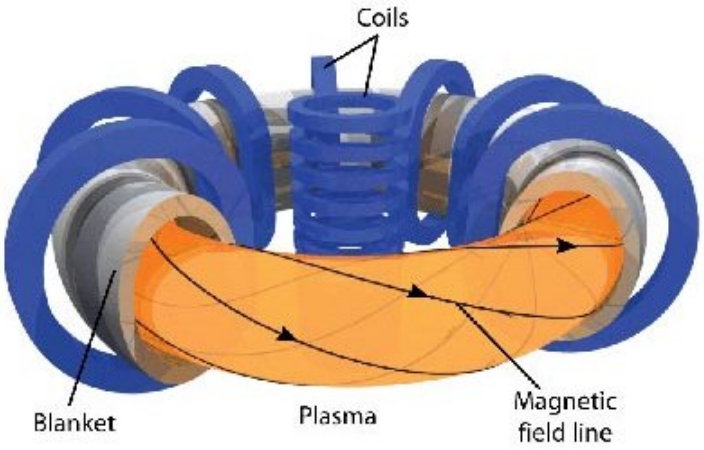

Figure 1.2: Schematic view of a typical tokamak. The plasma is confined by magnetic field line running helically around the toroidal axis. Picture from [2].

poloidal magnetic field. The plasma itself, which is an excellent electric conductor, is the secondary loop, and so has a large current induced in it. This plasma current produces heat, just as a wire warms up when an electric current flows through it. Tokamaks largely rely on plasma current not only for heating, but mostly for the poloidal magnetic field. As a result of the curl of the toroidal electric field this method can only work temporarily. This is clear from Maxwell's equation $\nabla \times \mathbf{E} = -\partial \mathbf{B}/\partial t$, which states that a constant electric field can only be maintained by a time-varying magnetic field.

At the densities and temperatures reached in fusion plasmas, significant kinetic pressure is obtained in the plasma core and large pressure gradients produce strong forces on the plasma. The ∇p forces are balanced by $\mathbf{j} \times \mathbf{B}$ forces arising from the magnetic field interacting with toroidal and poloidal plasma currents. This force balance is often called the magnetic equilibrium of a plasma configuration.

1.2.2 Additional heating and current drive

To reach *ignition*, a self sustained plasma by power release from its own fusion reactions, the fuel must be heated to hundreds of million degrees. Sustaining the plasma at this temperature requires control of its density and minimization of heat losses. As a result from any electron heating process, the resistance decreases with the temperature as $T_e^{-3/2}$, where T_e is the electron temperature. This means that in the beginning of a discharge, Ohmic heating is a convenient heating method, but at higher temperatures the heating method becomes inefficient and additional technologies must be implemented, e.g. neutral beam injection (NBI) or resonant interaction between particles and electromagnetic waves such as the electron cyclotron (EC) wave, the ion cyclotron (IC) wave, the lower-hybrid (LH) wave, etc. Both NBI and radio-frequency (RF) wave injection are non-inductive heating method that can sustain a steady-state plasma.

In NBI high energy neutral particle beams are injected into the plasma to transfer their energy to the plasma ions. By accelerating ions with high voltage that are converted into neutral atoms just before the injection the particle beam is generated.

Charged particles orbits in a tokamak are characterized by three periodic motions and their respective frequencies : the gyro-frequency for the rotation around field lines, the bounce- or transit frequency for the parallel motion along the field lines, and the drift frequency. By appropriately choosing the frequency and the launching characteristics of RF waves, it is possible to control the resonant interaction of these waves with electrons or ions. Particles of specific species and characteristics (location, energy, magnetic moment) can thus be targeted by controlled RF heating.

1.3 Lower hybrid current drive

Current drive in a tokamak refers to the production of a toroidal electric current flowing inside the plasma to generate a poloidal magnetic field. For years lower hybrid current drive (LHCD) has proven to be an efficient non-inductive current drive system with great prospects for future tokamaks. One of its main advantages is its capability to drive off-axis current in long pulse operation, which is useful for suppressing magnetohydrodynamical (MHD) instabilities and to enable continuous operation. Ever since the first demonstration of the flexibility of lower hybrid waves in the Japanese JFT2 [3] and American PLT [4] the LHCD technology has been developed and used in several tokamak experiments.

In a future fusion reactor, the plasma current and its profile should be controlled by non-inductive methods to complement the self-generated bootstrap current. Better energy confinement is obtained with a hollow safety factor profile with a region of negative magnetic shear, which requires off-axis (not in the center of the plasma) current drive sources. Unlike the electron cyclotron wave, the lower hybrid waves maintains a high current drive efficiency when the power is deposited far off-axis.

Lower hybrid waves, in the frequency range between ion and electron cyclotron frequencies ($\omega_{ic} < \omega_{LH} < \omega_{ec}$), interact with electrons via Landau damping using the slow wave polarization. This wave propagates with a a small angle with respect to the magnetic field lines and can encircle the torus several times before reaching the plasma center. The frequency band of lower hybrid waves reaches between 1 and 8 GHz, corresponding to free space wavelengths in the microwave region. For lower hybrid waves to propagate in the plasma, the density must at least be on the order of $10^{17}\,\mathrm{m}^{-3}$.

The LH current drive efficiency is defined as

$$\eta_{20} = \frac{n_{20} \cdot R \cdot I_{LH}}{P_{LH}} \tag{1.5}$$

where n_{20} is the central electron density expressed in units of $10^{20}\,\mathrm{m}^{-3}$, R the tokamak major radius, I_{LH} the LH driven current and P_{LH} the input LH power. [5]

The LH current (I_{LH}) can be driven with or without the presence of inductive current.

The total plasma current (I_p) may be decomposed as

$$I_p = I_{ohm} + I_{LH} + I_{hot} + ... \tag{1.6}$$

The first term is the pure inductive Ohmic part, $I_{ohm} = V_{loop}/R_{sp}$, V_{loop} is the loop-voltage and R_{sp} is the Spitzer resistance. The pure non-inductive part is $I_{LH} = \eta_0 P_{in}/n_e R$. If the loop voltage is negligible, the scenario is close to *full current drive* and the first term in Equation 1.6 is negligible. Cross terms between inductive and non-inductive current exists when both $V_{loop} \neq 0$ and $P_{LH} \neq 0$. The first cross term is $I_{hot} = V_{loop}/R_{hot}$ and the higher order terms are proportional to $P_{in}V^2$, VP_{in}^2, $P_{in}^2V^2$ and so on. The hot resistivity R_{hot} is inversely proportional to $\int \sigma_{hot}\,\mathrm{d}S$. [6]

1.3.1 Landau damping

Landau damping occurs due to energy exchange between an electromagnetic wave and particles in the plasma with a velocity close to the phase velocity (v_{ph}) of the wave. The particles interact strongly with the wave and will be accelerated if they are moving slightly slower than v_{ph}. In the same way particles moving faster than v_{ph} will lose energy to the wave and slow down. The motion along the magnetic field is possible if the wave has an electric field component parallel to the magnetic field line and its phase velocity component ($\omega/k_\parallel$) fulfills the resonance condition

$$v_\parallel - \omega/k_\parallel = 0 \tag{1.7}$$

If there are more particles with velocity smaller than v_{ph} than faster particles, the number of particles that gain energy will be larger than the number of particles losing energy. In other words, the wave is damped and the plasma is heated. In addition, an asymmetry in velocity distribution results from the resonance condition (1.7), which generates a net electric current, see Figure 1.3.

The resulting current drive efficiency is inversely proportional to the plasma electron density (n_e) and the square of the parallel refractive index ($n_\parallel = ck_\parallel/\omega$) [7].

1.3.2 Spectral properties of launched wave

The LH power waves are launched from the launcher grill, consisting of active waveguides possibly alternated by passive waveguides that are not fed with power from the klystrons. The shape of the power spectrum depends on the waveguide array configuration and dimensions.

Fourier transform of active waveguides into $n_\parallel$ space gives the power spectrum, where $n_\parallel$ is the refractive index parallel to the applied magnetic field. The positions of the peaks, for positive and negative $n_\parallel$ can also be calculated. The obtained spectrum then couples to the plasma depending on the plasma properties. By dividing a waveguide into a given number of secondary waveguides (N) one obtains a multi junction grill that divides the incident power along the toroidal direction. The phase shift between each

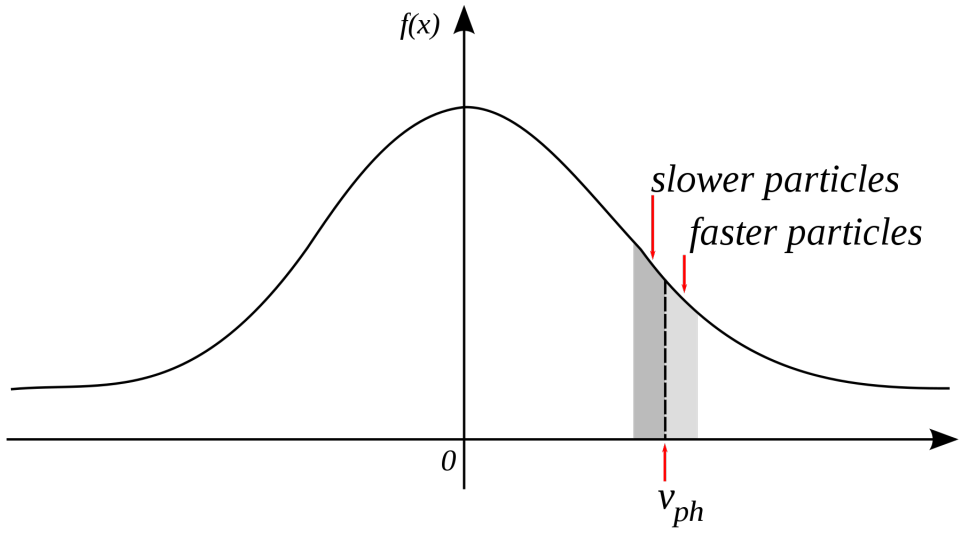

Figure 1.3: Due to the asymmetry in velocity distribution there are fewer particles with velocity higher than the phase velocity of the wave v_{ph} which results in a net electric current. Picture from [1].

resultant wave is obtained by a suitable reduction in the height of the waveguides. The power spectrum is given by the following relation:

$$\frac{dP}{dn_{\|}} = \frac{Y_0}{\lambda_0} L^2 sinc^2(n_{\|} k_0 L/2) \left(\frac{\sin(N\Phi/2)}{\sin \Phi/2} \right)^2 \left(\frac{\sin(M(N\Phi - \delta\Phi)/2)}{\sin(N\Phi - \delta\Phi)/2} \right)^2 \tag{1.8}$$

where $\Phi = n_{\|} k_0 L - \Delta\phi$, M is the number of modules that the launcher consists of and $sinc(x) = \frac{sin(x)}{x}$. The launcher will operate with a phase shift ($\Delta\phi$) between two active waveguides of a module giving a parallel refractive index defined by the distance between the active waveguides (L)

$$n_0 = \frac{\Delta\phi}{k_0 L} + \frac{\delta\Phi}{N_{wg} k_0 L}, \tag{1.9}$$

where N_{wg} is the number of active waveguides per row of the module.

Contrary to the phase shift $\Delta\phi$ between two active waveguides of a module, which is fixed by waveguide geometry, the phasing between two adjacent modules $\delta\Phi$ can be changed, by modifying the phase at the klystron, which results in changed parallel wave number at the power peak value. This means that the $n_{\|}$ is fixed around the design value, set by geometry, with some degree of flexibility by modifying the nominal phase shift between two modules.

The *directivity* of the launcher compares the radiation intensity in a particular direction, parallel and antiparallel to the magnetic field, with the total radiated power. In our case, it is useful to define the directivity as the ratio of the part of the spectra with

co current driving $n_\parallel$ over the total power. Waves with $|n_\parallel| < 1$ cannot couple to the plasma, therefore the limit of integration starts from $|n_\parallel| = 1$.

$$D = \frac{1}{P}\int_1^\infty P(n_\parallel)\mathrm{d}n_\parallel \tag{1.10}$$

Since the driven current is proportional to the inverse square of $n_\parallel$, in addition to the above definition of directivity, it is also useful to quantify the quality of the spectra, by defining a $n_\parallel^2$ weighted directivity (D_{cd}) according to the following equation:

$$D_{cd} = (1 - RC) \times \frac{n_\parallel^2}{P}\left(\int_1^\infty \frac{1}{n_\parallel^2}P(n_\parallel)\,\mathrm{d}n_\parallel - \int_\infty^{-1} \frac{1}{n_\parallel^2}P(n_\parallel)\,\mathrm{d}n_\parallel\right), \tag{1.11}$$

where RC is the average reflection coefficient in front of the launcher modules and P is the power density.

An RF wave that is not hindered by edge cutoffs can propagate into a plasma. In general, the wave power is damped by resonant interaction before reaching a perpendicular wave resonance. The absorption coefficient depends on

- the number of electrons with a parallel velocity near the wave phase velocity,
- the slope of the velocity distribution function of the resonant particles, and
- the relative amplitude of the electric field.

The electrostatic nature of slow LH waves yields a relatively large electric field amplitude and a strong interaction with electrons via Landau damping.

1.4 Kinetic description of plasma

The basic difference between a gas and a plasma is that a plasma is composed of charged particles, which react to electromagnetic forces. To capture the physics of LHCD, a *kinetic model* is used by calculating the distribution of phase space and velocity. The electromagnetic fields that determine the forces on each particle are functions of the charge and current distributions in the plasma, and hence of the distribution function itself. Therefore the solution of the kinetic equation is very complicated even in the collisionless limit. Since the resonant wave particle interaction of LHCD depends on the momentum-space distribution of the particles, kinetic theory of the plasma is necessary. In this section a kinetic description of the electrons and radio frequency waves is given.

The most complete description of a plasma composed of N particles would rely on the solution of the 3N equations of motion where the calculation of the force acting on each particle has account for the influence of all the other particles in the system. Such calculations are not reasonable and moreover would generate a lot of unnecessary information about the microscopic behavior of every particle in the system. Since we are interested in macroscopic quantities like density, temperature and currents, a statistical approach is required.

The evolution of the electron distribution in a plasma is governed by the Fokker-Planck equation, which is a convection-diffusion equation in phase space. It describes the multiple scattering process of the particles in a plasma. Besides collisions, the formulation can describe wave-plasma interaction and the force on the particles in an electric field. In plasma physics the Fokker-Planck equation is fundamental in heating, current drive, radiation emission and runaway electron dynamics.

The lower hybrid waves and the distribution function are solved self-consistently by solving a non-linear system where the RF waves fulfill Maxwell's equations:

$$\nabla \times \mathbf{E} = -\frac{\partial \mathbf{B}}{\partial t} \tag{1.12}$$

$$\nabla \times \mathbf{B} = \mu_0 \mathbf{J} + \frac{1}{c^2}\frac{\partial \mathbf{E}}{\partial t} \tag{1.13}$$

The effect of the LH waves on the plasma depends on the phase-space particle distribution. The current is given by

$$\mathbf{J}(\mathbf{x},t) = e \iiint \mathbf{v} f(\mathbf{x},\mathbf{p},t)\, \mathrm{d}^3 p, \tag{1.14}$$

where $f(\mathbf{x},\mathbf{p},t)$ is is the distribution function, with $\mathbf{x}$ being the position in configuration space and $\mathbf{p}$ is the momentum. The number of particles in the volume element around the point $\mathbf{z} = (\mathbf{x}, \mathbf{p})$ at the time t is given by:

$$\int f(\mathbf{x},\mathbf{p},t)\, \mathrm{d}^3\mathbf{p}\, \mathrm{d}^3\mathbf{x} = N. \tag{1.15}$$

The movement of the particle in the plasma can be expressed as $\dot{\mathbf{z}} = (\dot{\mathbf{x}}, \dot{\mathbf{p}})$. Being a particle density in phase space, the distribution function must satisfy a continuity equation, expressing that the total number of particles must be conserved:

$$\frac{\partial f}{\partial t} + \frac{\partial}{\partial \mathbf{z}}(\dot{\mathbf{z}} f_\alpha) = 0, \tag{1.16}$$

which is known as the Vlasov equation:

$$\frac{\partial f}{\partial t} + \mathbf{v} \cdot \nabla f + \dot{\mathbf{p}} \cdot \frac{\partial f}{\partial \mathbf{p}} = 0. \tag{1.17}$$

We add the binary collision operator $C(f,f_\alpha)$ to describe the Coulomb collisions, where α denotes all plasma particles, including the electrons. The Fokker-Planck equation is the Vlasov equation with the effects of small scale fluctuations gathered in a collision term on the right hand side:

$$\frac{df}{dt} = \frac{\partial f}{\partial t} + \mathbf{v} \cdot \nabla f + \dot{\mathbf{p}} \cdot \frac{\partial f}{\partial \mathbf{p}} = C(f,f_\alpha). \tag{1.18}$$

In Equation (1.18), $\dot{\mathbf{p}} = e\,(\mathbf{E} + \mathbf{v} \times \mathbf{B})$ is the Lorentz force acting on the electrons from both constant equilibrium and oscillating radio frequency electromagnetic fields.

Despite their rather compact form, Equation (1.17) and (1.18) are normally not easy to solve. This is essentially due to the fact that the forces acting on the system can depend in complicated ways on the distribution function itself. This makes these equations, in general, nonlinear integro-differential equations.

In a typical plasma we can approximate the collision operator $C(f,f_\alpha)$ so that particle diffusion and drag results from the cumulative effect of small angle scattering but neglecting scattering of large order angle. If the particle distribution function remains close to a Maxwellian distribution, the Fokker-Planck operator can also be linearized. In the code used in this master thesis, a linearized, momentum-conserving, bounce-averaged relativistic Fokker-Planck equation is implemented to describe a collisional plasma, where electrons collide with ions, neutral molecules or other electrons. The Fokker-Planck equation balances collisions, quasi-linear diffusion by RF waves, radial transport and acceleration by a toroidal electric field.

1.5 Outline

This thesis investigates the current drive efficiency of the radio frequency waves in the lower hybrid regime in the Tore Supra tokamak under high power conditions. Due to limitations in plasma measurement and the lack of methods to measure the current profile in tokamaks, simulations are essential in the search for understanding and development of RF current drive.

A suite of codes specifically coupled and optimized for LHCD modelling is used, including a code for equilibrium and transport (METIS) [8], LH wave coupling to the plasma (ALOHA) [9], LH wave propagation (C3PO) [10], electron distribution (LUKE) [11] and fast electron bremsstrahlung emission reconstruction (R5X2) [12]. The codes of the suite will be introduced in Chapter 3.

The simulation results, such as current drive efficiency, are analyzed and compared to experimental results. The plasma equilibrium and kinetic profiles are defined by METIS simulations, providing magnetic equilibrium, the plasma density and temperature profile. The plasma is a highly non-linear medium, which means that small perturbations of the equilibrium can affect the current drive considerably.

Coupled to the codes and given the input, the 3D bounce averaged relativistic Fokker-Planck solver LUKE computes the electron distribution. Full convergence is obtained in the self-consistent calculation of the wave damping and distribution function. The simulation results are then compared to experimental data from the Tore Supra tokamak. Validation and optimization of the code for LH scenarios is done by testing a wide range of parameters through systematic scans.

In the Tore Supra tokamak, LH waves are coupled to the plasma by a Full Active Multijunction (FAM) launcher and/or a Passive Active Multijunction (PAM) launcher. The later one was installed to test an ITER relevant launcher design [5]. Detailed spectra based on experimental measurements of phase and LH power are generated for each Tore Supra scenario and launcher in the ALOHA code. A number of discharges have been performed in Tore Supra involving the two launchers, in a variety of plasma conditions

including full current drive. The effect of the $n_{\|}$ spectrum on the LH current drive efficiency for the Passive Active Multijunction (PAM) is well demonstrated under full current drive scenarios.

The ray-tracing code (C3PO) uses the ALOHA generated LH wave spectrum as input. The spectral properties of the launched wave, that is the coupling between waveguide modes and plasma admittance, is modelled in ALOHA yielding launcher power spectrum as a function of the parallel (to the magnetic field) refractive index. The reflection coefficient depends on the plasma density at the launcher mouth which is specified based on experimental measurements. Since handling the full LH spectra obtained from ALOHA in LUKE would be very time consuming, the spectra need to be simplified without losing details significant for the current drive. The number of rays in a wave used in the LUKE simulations is given by the product of *number of lobes* in the launcher spectrum *number of vertical positions* the simplified spectrum is launched into the plasma. A systematic scan of the number of poloidal launch positions and number of $n_{\|}$ values used in the ray-tracing calculations is done. The propagation of rays from the spectra are calculated with the ray-tracing code C3PO. It is found that 36 rays, corresponding to the six waveguide rows and the six main lobes in the LH spectrum, are sufficient to describe the LH wave propagation from FAM and PAM launcher.

The LHCD launchers FAM (C3) and PAM (C4) have shown different results in Tore Supra experiments with the same main parallel refractive index of the launched wave. Comparison of the LH driven current profile and hard X-ray emission profile for the Full Active Multijunction (FAM) launcher and the PAM launcher in full current drive is made. This comparison illustrates the effect of the launched $n_{\|}$ spectrum on LHCD.

The driven current calculated by LUKE and a synthetic diagnostic of the bremsstrahlung emission from supra thermal electrons by the code R5X2 enables a comparison of the LHCD simulation with experimental measurements. Excellent agreement between the simulated and experimental HXR emission is obtained for the full current drive discharge at relatively low density ($n < 2 \times 10^{19}\,\mathrm{m}^{-3}$) , both in absolute amplitude and shape of the profile. Comparison between simulations and HXR profile also gives an idea on the extent of radial transport of fast electrons, a well debated topic in fusion research.

2

LHCD in Tore Supra

With the mission to study the physics and technology of a steady-state tokamak, Tore Supra is situated at the nuclear research center of Cadarache in France where it operates since 1988. As one of the largest tokamaks in the world, it involves the use of superconducting magnetic field coils, water cooled plasma facing components and long-pulsed non-inductive current drive system. See Figure 2.1 for an outside and inside view of the machine.

For the purpose of long pulse discharges, Tore Supra is equipped with two LH launchers designed to drive current during 1000 s long pulses. Among tokamaks, Tore Supra holds the record of injected energy, with LH power alone, with totally 1 GJ from a six minute long discharge [13]. The overall world record of injected energy is held by the Large Helical Device (LHD) stellarator (1.6 GJ) [14].

Ever since the start up, LHCD has been an important part of the research at Tore Supra. Its well developed system for non inductive current drive is described in this chapter.

2.1 The LHCD system

LHCD has been used in Tore Supra for current drive for more than 20 years. Over the years, different launcher concepts have been tested. A new LHCD launcher that relies on a periodic combination of active and passive waveguides was installed in Tore Supra in 2009 [15], [16]. The design allows active cooling of the launcher, necessary for ITER like conditions [17]. Designed with ITER-relevant scenarios in mind, the Passive Active Multijunction (PAM) allows efficient active cooling of the waveguides, necessary for long pulse operation [18], [15]. The PAM launcher has shown encouraging experimental results, with reflection and power handling that correspond to the expectations [5].

As a complement to the PAM launcher an older launcher of different design is still installed in Tore Supra. The Fully Active Multijunction (FAM), consists of only active

(a)

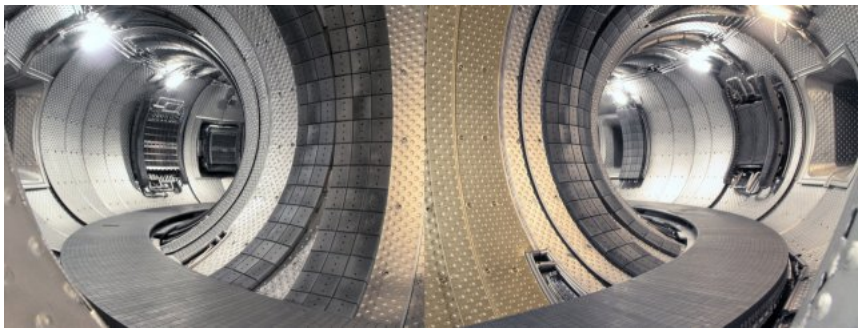

(b)

Figure 2.1: Outside and inside view of the Tore Supra tokamak.

waveguides inside each module with a passive waveguide inserted between each module. See Figure 2.2. The two launchers in Tore Supra are denoted C3 (the currently installed FAM launcher) and C4 (the PAM launcher). See Figure 2.3 for a view of the launchers from the inside of the tokamak. Before the PAM launcher (C4) was installed in Tore Supra, there was instead an additional FAM launcher with four waveguide rows in use (denoted C2).

The launcher consists of 16 modules with eight active and eight passive waveguides each. The multijunction design results in low power reflection ($RC < 2\%$) [18] from the plasma for densities near cut off ($1.7 \cdot 10^{17}$ m^{-3} at $f = 3.7$ GHz) in front of the launcher mouth. This makes PAM type launchers very advantageous for ITER, where the density at the launcher mouth is low due to significant distance between the plasma edge and the wall.

The lower hybrid wave launchers have been designed for long pulse operation, which is essential for research on steady-state plasma control, like current diffusion and plasma-wall interaction. The multijunction launchers, also known as *grills*, consist of phased

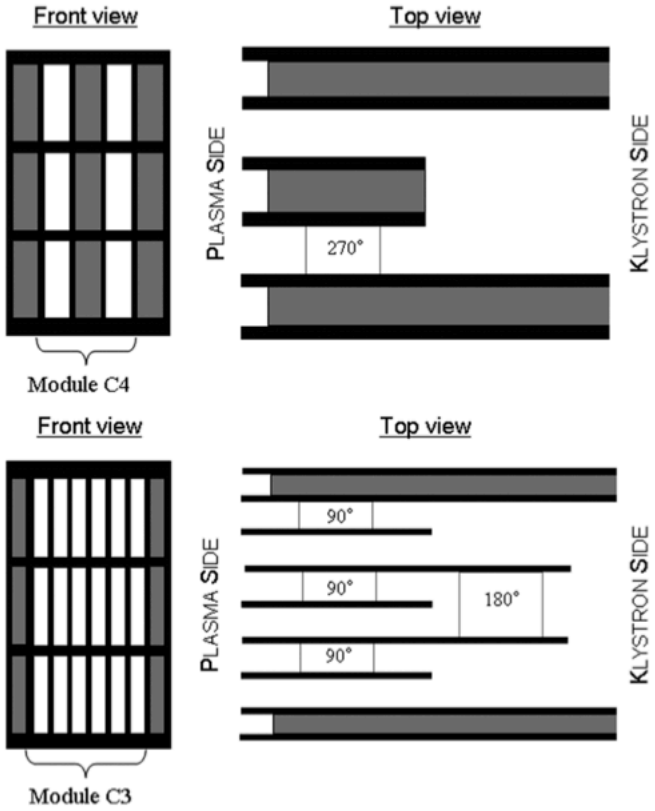

Figure 2.2: Schematic front and top view of C4 (top) and FAM C3 (bottom). The grey rectangles correspond to *passive* waveguides and the white rectangles to *active* waveguides. Each module consists of three rows of waveguides. Figure from [19].

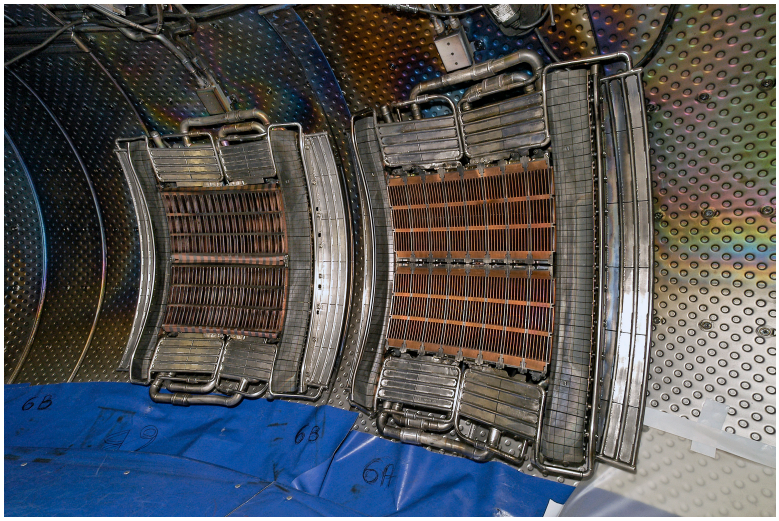

Figure 2.3: C4 (left) and C3 (right) launchers seen from inside of Tore Supra.

arrays of waveguides that produce waves traveling with phase velocity $v_\parallel = c/n_\parallel$ parallel to the magnetic field. The resulting wave is launched with a spectrum of velocities, for convenience expressed in $n_\parallel$. The mathematical description of the power spectrum was given in Section 1.3.2, but let us apply the expression to the C4 launcher. The main features of the power spectrum is fixed by geometry, but the peaks of the spectrum have some flexibility by modifying the nominal phase shift between two modules. The main peak, $n_\parallel^{peak}$, of the launched power spectrum for C4 can be slightly tuned according to the expression:

$$n_\parallel^{peak} = \frac{\Delta\phi}{k_0 L} + \frac{\delta\Phi - 180^\circ}{N_{wg} k_0 L \times \frac{180}{\pi}} = 1.72 + \frac{\delta\Phi - 180^\circ}{313.2^\circ} \tag{2.1}$$

where

- the number of waveguides is $N_{wg}^{C4} = 2$,
- $k_0 = 77.54 m^{-1}$ at the operation frequency 3.7 GHz,
- the geometric periodicity of the waveguide array: $L^{C4} = 35.25\,\text{mm}$,
- the phasing between two active waveguides of a module in C4 is $\Delta\phi = 270\,^\circ$.

The nominal phase shift is $\delta\Phi = 180\,^\circ$ for the C4 launcher. At this phasing the *directivity*, the ratio between co driving LH power and total incoming power, is maximized around the cut-off density [19]. In other words, the C4 launcher is most efficient for a main peak centered around $n_\parallel = 1.72$, but for other launchers it can be a different value. As an example, C3 is optimal for current drive with phasing such that the main power has $n_\parallel = 2.0$.

The power of the lower hybrid system is generated by 16 klystrons, eight for each launcher, operating at 3.7 GHz. Transmitted through about 20 meter of copper waveguides to the edge of the tokamak, the power is split in two by each waveguide in a 3 dB hybrid junction. This gives 16 transmission lines for each launcher, out of which eight lead to the upper and eight to the lower part of each launcher. Of the 16 transmission lines, eight lead to the upper and eight to the lower part of the launcher. Mode converters (TE10 to TE30) divide the incoming power into three poloidal rows for each of the two half launchers. The waveguide modules are connected to the tokamak through double BeO windows. Figure 2.4 gives a general overview of the setup.

2.2 LHCD diagnostics

In this section I will introduce the most relevant diagnostics tools to this thesis. For a more complete description of the diagnostics and plasma, see [20].

(a) Front view of the waveguide modules of C4 before installation.

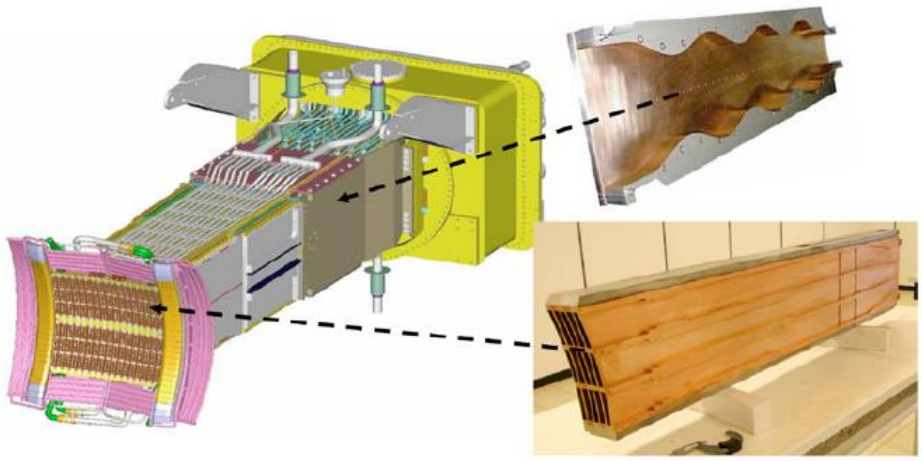

(b) Complete PAM type launcher setup. Mode converter and PAM module.

Figure 2.4: View of C4 launcher, pictures from [18]. The whole launcher weighs 8 tonnes.

2.2.1 Hard X-ray spectroscopy

Measurements of fast electron bremsstrahlung (FEB) generated by the LHCD in the hard X-ray (HXR) photon energy range (3-200 keV) is used for analysis of the fast electron dynamics in a tokamak plasma. In Tore Supra the detectors span the tokamak and provide an HXR profile that can be used to calculate the Bremsstrahlung photon temperature emitted by the fast electrons.

Hard X-ray (HXR) fast electron bremsstrahlung tomography is an important diagnosis tool for analyzing the lower hybrid wave dynamics in Tore Supra. The tomographic setup DVSPX detects the supra thermal emission created by resonant interaction with lower hybrid waves from the fast electrons in the range $20 - 200$ keV and gives their location and energy. The dynamics of the electron distribution can be used for measurements of the LH power deposition.

The diagnostics consists of one vertical and one horizontal camera equipped with neutron shielding and respectively 21 and 38 cadmium telluride (CdTe) detectors each, see Figure 2.5. Each detector measures the X-ray emission in a poloidal section of the plasma, integrated along the line of observation and given the detector response function, a count rate signal can be found for each cord. Abel inverted HXR emission has routinely been used in the energy range $60 < E < 80$ keV as a relative measurement of the radial current profile for the lower hybrid driven current in Tore Supra. The amplitude is rescaled by some current drive model.

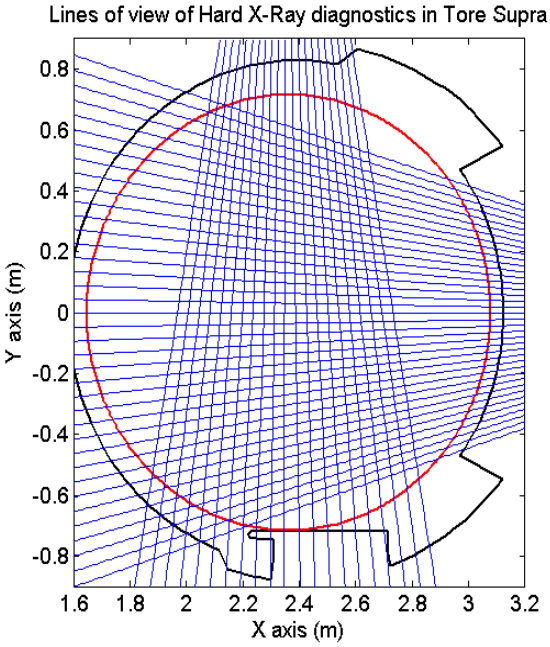

Figure 2.5: Schematic view of the hard X-ray detector setup. The lines of sight of the detectors, also called chords, are marked in blue.

2.2.2 Edge density measurement

Langmuir probes are among the oldest plasma diagnostics with still high importance. The Langmuir-probe is a tiny metallic electrode in direct contact with the plasma. Depending on the potential applied, the small electrode either injects or extracts charged particles from the plasma. Currents to the probe are governed by the electron density and the electron temperature as well as the plasma potential. All three quantities can be derived from the measured current-voltage characteristic of the probe, which is obtained conducting a fast voltage sweep.

Eight Langmuir probes, placed in the corners of each of the two launchers, see Figure 2.6. They measure the local plasma density in front of the launchers. To protect the

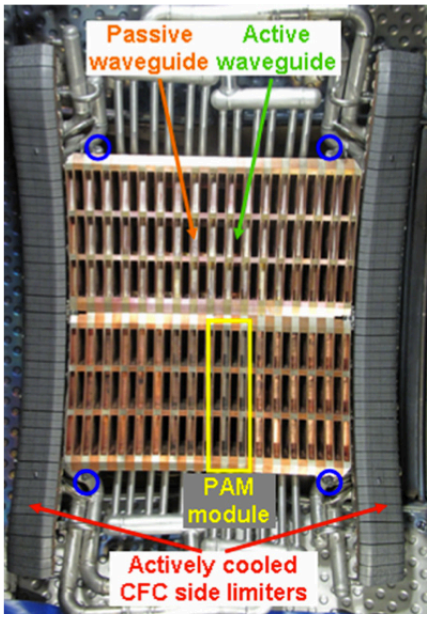

Figure 2.6: Photo of C4 launcher mouth. The four blue circles show the location of the Langmuir probes. The yellow rectangle shows a PAM module, which holds six active and six passive waveguides. Picture from [5]

launcher from high heat and particle flux the front of the launcher is positioned in the scrape off layer (SOL). There is also two lateral protection components installed for protection (limiters) placed a distance $d = 2\,\text{mm}$ from launcher face. The layer of a low density plasma between the launcher face and the limiters is called *private plasma*. The Langmuir probes measure somewhere in the private plasma that is formed between the LH launcher mouth and the scrape off layer (SOL), see Figure 2.7(a). In the private plasma layer the density varies like

$$n(x) = n_{Langmuir} e^{\frac{(x-d)}{\lambda}}, \tag{2.2}$$

where x is the position relative to the launcher mouth, $d = 2\,\text{mm}$ the distance between the SOL and the launcher mouth and λ is the density gradient ($\lambda = 2\,\text{mm}$ is used in the

ALOHA calculations), see Figure 2.7(b). The density at the launcher mouth can thus be assumed to be between $n_{Langmuir}/e$ and $n_{Langmuir}$. Current drive calculations can be expected to be very sensitive to such a density error, since the $n_{||}$ weighted directivity and reflection coefficient varies significantly in the relevant density region, see Figure 2.8.

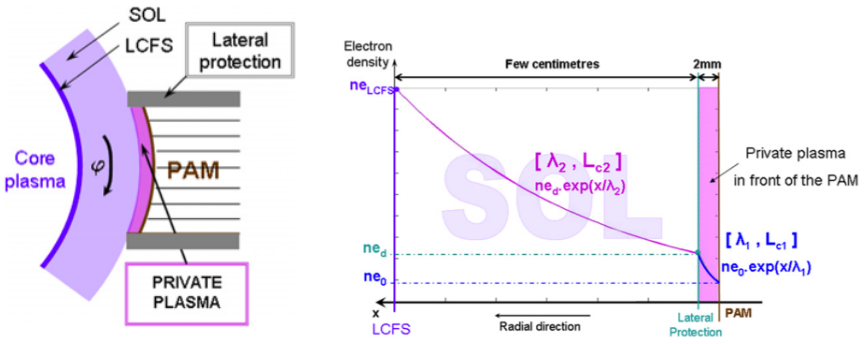

(a) (b)

Figure 2.7: (a) Toroidal view of the first private plasma region, limited by the two lateral protections. (b) Electron density profile in front of the LH launcher, with two plasma layers. The Langmuir probe measures the density somewhere in the private plasma (in purple). Figures from [19].

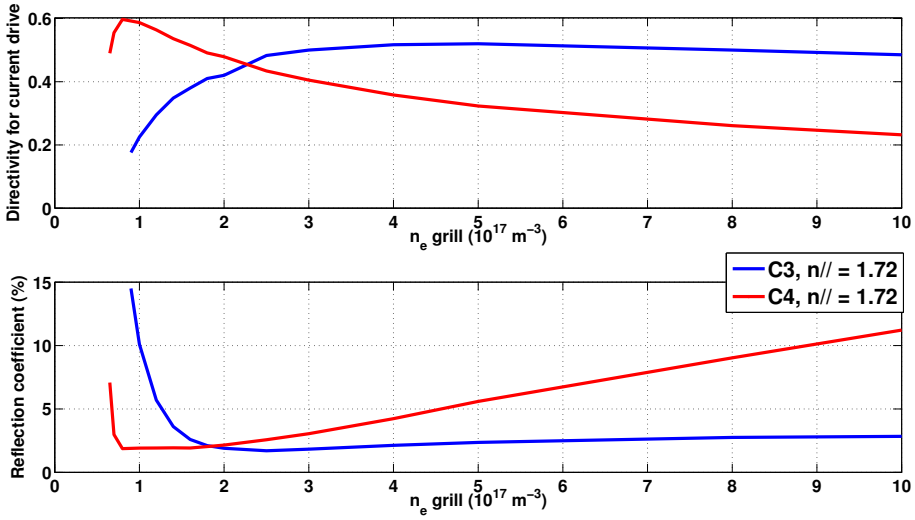

Figure 2.8: The directivity for current drive and reflection coefficient for C3 (blue) and C4 (red) launcher with module phasing corresponding to a main parallel refractive index at 1.72, calculated in ALOHA.

3

Simulation tools

In order to study the dynamical phenomena in plasmas, computer simulations are necessary to implement the theoretical models and calculate variables that can be compared to experimental observations. Especially in the field of lower hybrid current drive, where there are no methods to experimentally measure the current profile, which is a key parameter for controlling MHD activities in the plasma. To model the results of LHCD experiments the theory behind three physical processes that follow the current drive process from the wave insertion to the power absorption must be implemented:

- coupling between the LH wave launcher (a phased waveguide array) and the edge plasma,
- propagation of the coupled LH wave until it reaches the absorption region,
- efficiency of the absorption process.

In this chapter, the principles of the modelling procedure is described and an introduction to the codes is given. The modelling scheme for modelling the electron distribution function of momentum and configuration space is described below and illustrated in Figure 3.1.

The LH waves are launched through multijunction waveguide arrays (described in Chapter 2.1) positioned near the plasma edge near the cut-off density. Simulations in the coupling code ALOHA provides a detailed LH spectrum coupled to the plasma, based on experimental data, such as edge density (n_{edge}), forward and reflected power and phasing of the launcher modules ($\delta\Phi$).

The TS database provides with input from experimental measurement of plasma current (I_p), net lower hybrid power (P_{LH}) and effective charge (Z_{eff}). Experimental based input data for each plasma scenario is generated in the METIS code that provides a suitable plasma equilibrium profile, defining the plasma parameters magnetic field strength ($\mathbf{B}$), density (n_α) and temperature profiles (T_e).

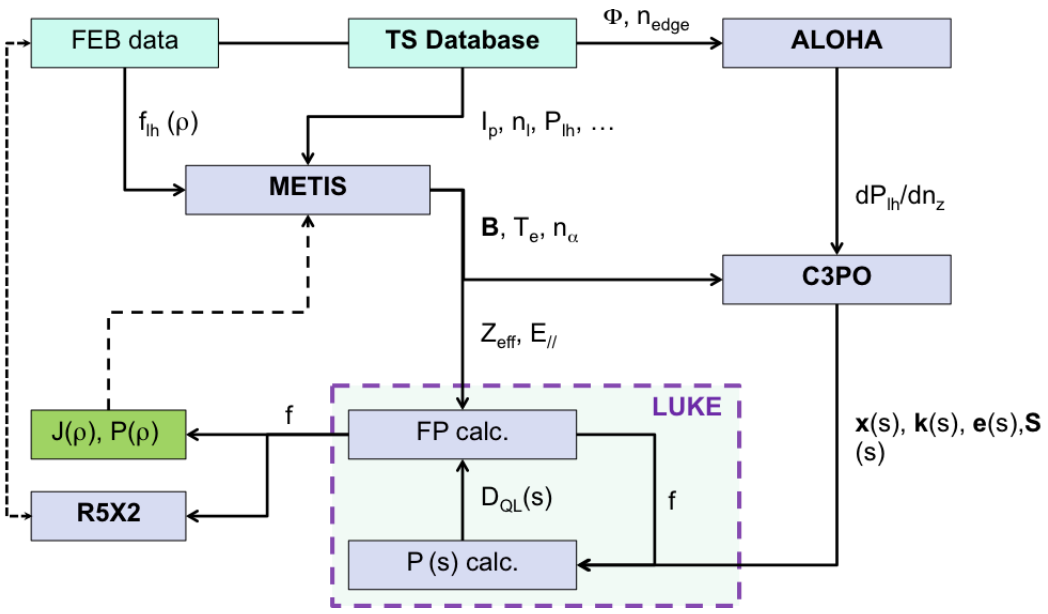

Figure 3.1: Work flow of the simulation routine, beginning from the Tore Supra database.

Provided with a power spectrum (dP_{LH}/dn_z) from ALOHA, the ray-tracing code C3PO calculates the lower hybrid wave propagation.

The deposition and current drive is calculated by the 3D bounce-averaged, i.e. integrated along the toroidal shape of the tokamak, relativistic Fokker-Planck solver LUKE. Finally, R5-X2 enables comparison of simulation results with experimental measurements, by reconstruction of the fast electron bremsstrahlung (FEB) in the hard X-ray domain.

3.1 Spectral modelling: ALOHA

The Advanced LOwer Hybrid Antenna (ALOHA) code models the coupling of LH slow (transverse) and fast (longitudinal) waves between the two dimensional radiating waveguide structure and the magnetized plasma edge. The output is a spectrum of parallel refractive index, see Figure 3.2. In our simulations we will use the ALOHA-1D version which calculates the coupling between wave guides one toroidal row of the launcher for the slow wave, as opposed to the ALOHA-2D version which calculates the coupling between all the waveguides for the slow *and* the fast wave. The 1D version is faster (minutes as opposed to hours) and agrees well with the 2D version in the type of scenarios in question [9].

The reflection coefficient is computed by treating the plasma as an antenna load. Given the phasing between two adjacent modules from antenna excitation data from the Tore Supra data base, the coupled lower hybrid spectrum is calculated. Any effect of reflected waves from the plasma core back to the waveguides is not taken into account.

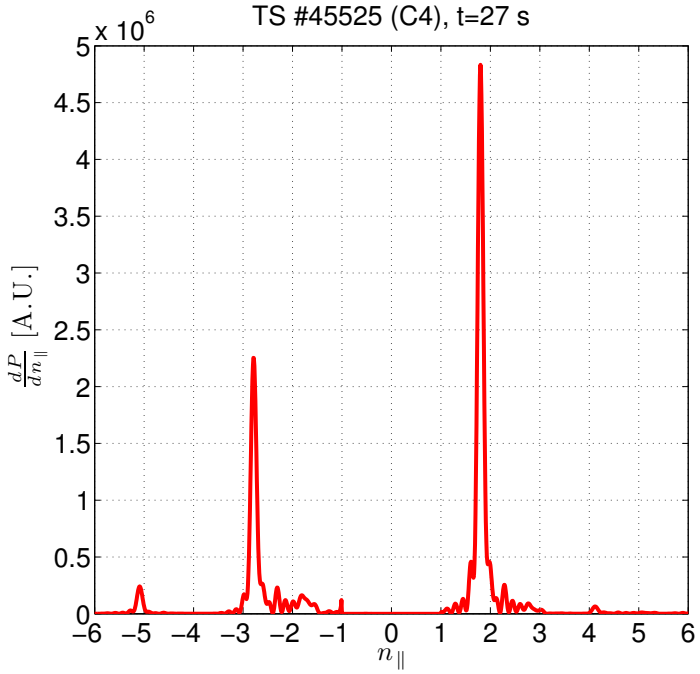

Figure 3.2: Example of spectrum calculated by ALOHA with a wave launched by the C4 launcher.

The antenna used in simulations is defined by waveguide dimensions, scattering matrices and module excitation. The user also needs to describe the plasma, by specifying the electron edge density profile defined by two density gradients, see Figure 2.7 in Section 2.2.2. When simulating a known scenario, the density can be estimated from diagnostics data from so called Langmuir probes or by matching the obtained reflection coefficient with experimental observations.

3.2 Equilibrium simulation: METIS

To get suitable equilibrium profile for a certain plasma scenario we use the fast integrated tokamak simulator for the CRONOS suite, called METIS (Minute Embedded Tokamak Integrated Simulator). CRONOS is a suite of numerical codes for integrated tokamak modelling of a full tokamak discharge. METIS provides interpretative simulations of TS discharges.

METIS solves a 1D stationary ODE transport equation, yielding particle and impurity densities, ion and electron temperatures, loop voltage, current density and plasma momentum. It also provides Ohmic radial profile, used for simulation of inductive pulses [8]. For full current drive scenarios the loop voltage is ignored, see Section 1.3 for motivation.

METIS computes the time evolution of the global plasma quantities for given wave-

forms of the control parameters. It solves the current diffusion equation taking an approximate equilibrium evolution into account. The current profile $J(\rho)$ is obtained by scaling the product of the current drive efficiency and the measured lower hybrid power by a form factor ($f_{LH}(\rho)$), either obtained from inverted HXR signal ($60 < E < 80\,\mathrm{keV}$) with radial dependence *or* prescription by the user. In the current drive calculations performed with the LUKE/C3PO platform in this work, plasma temperature and density is provided by METIS simulation output. The quality of the simulation is assessed by comparing the internal inductance (L_i) with experimental measurements. Figure 3.3 illustrates an example of the L_i calculated by METIS with the form factor given by inverted HXR profile.

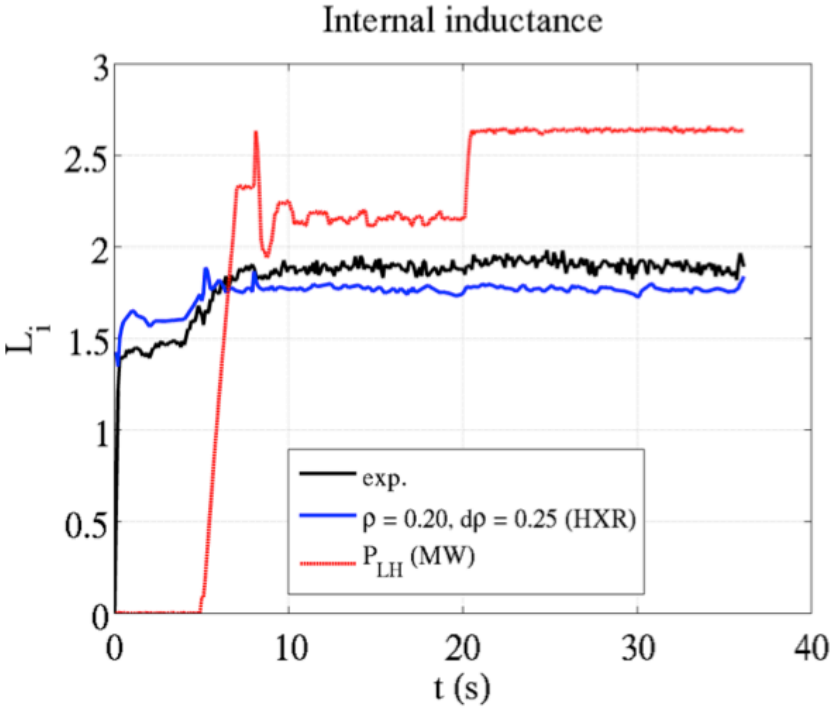

Figure 3.3: Example of internal inductance from METIS simulation compared to experimental measurement.

3.3 C3PO/LUKE

The C3PO/LUKE module is designed to treat RF electron resonant waves, like lower hybrid and electron cyclotron resonant waves. Both the raytracing code C3PO and the relativistic Fokker-Planck solver LUKE consider arbitrary axisymmetric magnetic equilibrium in a curvilinear coordinate system (ψ, θ, ϕ), where ψ is the poloidal magnetic flux, θ and ϕ are the poloidal and toroidal angles, respectively.

The propagation and *linear* absorption of the coupled LH waves in the tokamak is calculated with the C3PO code using a cold-plasma dielectric tensor. Calculations of the ray dynamics continue until all the RF power is expected to be linearly absorbed. In Tore Supra the damping rate of the LH wave is low and consequently damping effects are quasilinear. For ITER, this effect would be much smaller and the RF power is in a linear damping regime [21].

What distinguishes C3PO from many other ray-tracing codes (see for example [22]) is the choice of the curvilinear coordinate system that reflects the structure of magnetic flux surfaces in a magnetized toroidal plasma instead of more traditional toroidal coordinates (R, Z, ϕ). This results in faster and more accurate local interpolations, compared to a toroidal coordinate system [10].

For evaluations of all the derivatives in the ray-tracing, the magnetic equilibrium is expressed in a vectorial form using cubic splines and standard Fourier transformations. When the ray trajectories are calculated LUKE takes over and calculates the quasi-linear absorption of the LH power by self-consistently solving the power transport equation along each ray on the 2D fast electron distribution function in momentum space [11]. The 3D bounce-averaged Fokker Planck solver, LUKE, calculates the RF driven plasma current and *self consistent* power deposition. This is necessary since the damping of rays is intra and inter dependent for a non-Maxwellian distribution function. In other words, quasilinear effects arise when a ray interact with itself or other rays. The quasilinear effect can lead to either an increase in the wave damping rate (tail of fast electrons) or a decrease (flattening of the distribution).

The code uses a relativistic, momentum conserving, quasi-linear collision operator (D_{QL}) to calculate the electron distribution. The effect of trapped particles is also accounted for [21].

The wave equation for the RF fields $\widetilde{\mathbf{E}}(\mathbf{x},t)$ and $\widetilde{\mathbf{B}}(\mathbf{x},t)$, solved explicitly by C3PO looks like [11]:

$$\nabla_{\mathbf{x}} \times \nabla_{\mathbf{x}} \times \widetilde{\mathbf{E}} + \mu_0 \sigma(f) + \frac{\partial \widetilde{\mathbf{E}}}{\partial t} + \frac{1}{c^2} \frac{\partial^2 \widetilde{\mathbf{E}}}{\partial t^2} = 0 \tag{3.1}$$

where σ is the conductivity tensor that linearly operates on f. The distribution function $f(\mathbf{x}, \mathbf{v}, t)$ is calculated by numerically solving the a bounce-averaged guiding center Fokker-Planck equation:

$$\frac{\partial f}{\partial t} = \frac{\partial f}{\partial t}|_C + \frac{\partial f}{\partial t}|_E + \frac{\partial f}{\partial t}|_{RF} + \frac{\partial f}{\partial t}|_T \tag{3.2}$$

where the terms on the right hand side of Equation 3.2 represent:

- $\frac{\partial f}{\partial t}|_C$ is the collision operators of the collision terms between electrons and the different plasma species, including the electrons them self.
- $\frac{\partial f}{\partial t}|_E$ is the Ohmic field driven acceleration.
- $\frac{\partial f}{\partial t}|_{RF}$ is the term of wave-particle interaction.

- $\frac{\partial f}{\partial t}|_T$ is a term for radial transport proportional to D_r, a radial transport coefficient.

The Fokker-Planck equation balances all of these effects on the electron distribution. LUKE solves the Fokker-Planck equation by the finite difference method discretizing in phase space. The equation is of integro differential form that must be solved with an implicit time scheme for the differential terms and an explicit time scheme for the integral part. The FP equation takes the form of a linear equation system that is solved by LU factorization.

In the study of LH ray-tracing, the wave propagation can be divided into different propagation schemes that describe the path of the LH ray between launching and quasi-linear absorption. The type of absorption depends on the initial parallel refractive index of the launched wave ($n_{\|0}$), magnetic field strength and the plasma temperature and density profile.

The simplest case, in which the simulations are within the validity range, is the single pass absorption where the ray is absorbed without any reflections on the plasma edge. In multi pass absorption (MP) the wave propagates into the plasma but is reflected once or several times before reaching the absorption layer [21]. The case of one or two reflections is defined as few pass absorption (FP). In multi pass absorption with edge propagation (EP) the ray is confined by the accessibility condition near the plasma edge.

3.4 FEB reconstruction: R5-X2

To be able to verify the plasma processes described by the simulation suite, the results must be compared with measurement from diagnostics. Hard X ray spectroscopy provides information about the power deposition profile in the tokamak but a reconstruction of electron distribution from emission is not possible due to the complete mixing between angular, radial and momentum dependence of the fast electron tail, [11]. The HXR deconvolution is an ill conditioned problem, which makes R5-X2 an important synthetic diagnostics by reconstructing the FEB from the LUKE output, yielding a line integrated emission using the geometry of the HXR camera. The FEB reconstruction allows for comparison of count rate and photon temperature.

The code R5-X2 reconstructs the local emissivity of non-thermal bremsstrahlung from LH generated fast electrons in an arbitrary axisymmetric magnetic configuration using Legendre polynomial decomposition [12].

Bremsstrahlung emission in the HXR photon energy lies in the energy range $30 - 200\,\mathrm{keV}$, but due to Compton scattering effects and count rate statistics it is only relevant to detect photons in the energy range $50 - 110\,\mathrm{keV}$. In R5-X2 the bremsstrahlung emission is reconstructed as a function of chord number, so that it is directly comparable to the experimental HXR data.

4

Illustration of workflow

As an illustration of the modelling scheme the simulation workflow of a full current drive discharge performed in Tore Supra is described. In this example discharge with pulse number #45525 the plasma current is completely driven by the C4 launcher and $V_{loop} = 0$, in other words no flux consumption is present.

Plasma equilibrium and kinetic profiles based on experimental data from the Tore Supra database, are obtained with the METIS transport code. The coupling between launcher and plasma have been modelled in the coupling code ALOHA, yielding detailed LH spectra calculated from experimental measurement of waveguide power and relative phasing. The power spectra is obtained as a function of parallel refractive index ($n_{\parallel}$) launched by a single row of the LH launcher. The wave propagation is then calculated with the ray-tracing code C3PO and the power absorption by the self-consistent Fokker-Planck solver LUKE.

In this chapter, the modelling procedure from the coupling between the LH wave and the plasma to the power absorption is described, for the example discharge #45525. To draw general conclusions about the simulation suite and discuss the physical processes of LHCD a more statistical approach is used in Chapter 5 where results from several pulses, both fully and partially LH driven current, are presented.

Input power from the C4 launcher, total plasma current and plasma density at the grill is illustrated in Figure 4.1. At $t = 20$ seconds the phasing between the grill modules was changed from $\delta\Phi = -180\,^\circ$ to $\delta\Phi = -150\,^\circ$ which results in an increase of main $n_{\parallel 0}$ from 1.72 to 1.82 of the launched wave. The driven current is proportional to the inverse square of the parallel refractive index, thus the power must be increased to maintain the plasma current. The direction of the driven current, depends on the sign of the $n_{\parallel}$, where positive $n_{\parallel}$ drive a co current.

Aiming for efficient and precise LHCD calculations, only the most important features of the coupled LH spectrum from ALOHA are taken into account. In other words, the

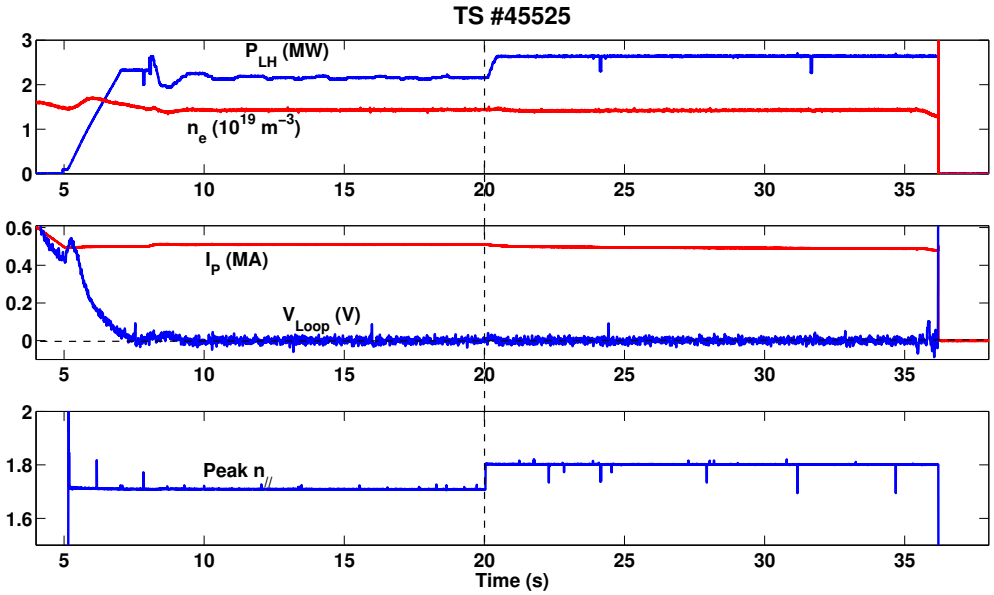

Figure 4.1: Data from discharge #45525. At 20 seconds into the discharge, the phasing between the modules is changed, resulting in less efficient wave. As a consequence the LH power is increased to maintain the plasma current.

spectrum is simplified by ignoring peaks that have negligible contribution to the plasma current. The electron distribution function is calculated by the Fokker-Planck solver LUKE yielding the radial current profile, which we show that for C4 driven cases can not be approximated by the available diagnostics. Full convergence is obtained in the self-consistent calculation of the distribution functions and power absorption along all rays.

A synthetic diagnostic of the fast electron bremsstrahlung emission is performed with the code R5X2. This reconstruction allows for a comparison between the simulation results and experimental measurements from the hard X-ray diagnostic system. Fast electron diffusion effects have been included in the Fokker-Planck analysis by introducing a radial diffusion operator in LUKE, see Section 3.3. For the full current shot #45525 and other low density scenarios ($n_e < 2 \times 10^{19}\,\mathrm{m}^{-3}$), excellent agreement with experimental HXR data is found. At higher densities, the wave propagation enters a regime where the calculations are questionable due to unrealistic wave propagation and inconsistency with experimental observations.

4.1 Spectral properties

The launched LH spectrum depends on the geometry and relative phasing of the modules of the launcher. The spectra of C4 and C3 are illustrated in Figure 4.2. One of the main features of the C4 spectra is the existence of a secondary lobe in opposite direction of

the main lobe, with negative $n_{\|}$ that carries a significant part of the power. This is a characteristic feature of waveguide structures where passive waveguides are positioned between the active waveguides. For ITER-like conditions, the passive waveguides are necessary to allow for a sophisticated cooling system. The effect of the spectral properties of the two types of launchers will be discussed in Chapter 5.

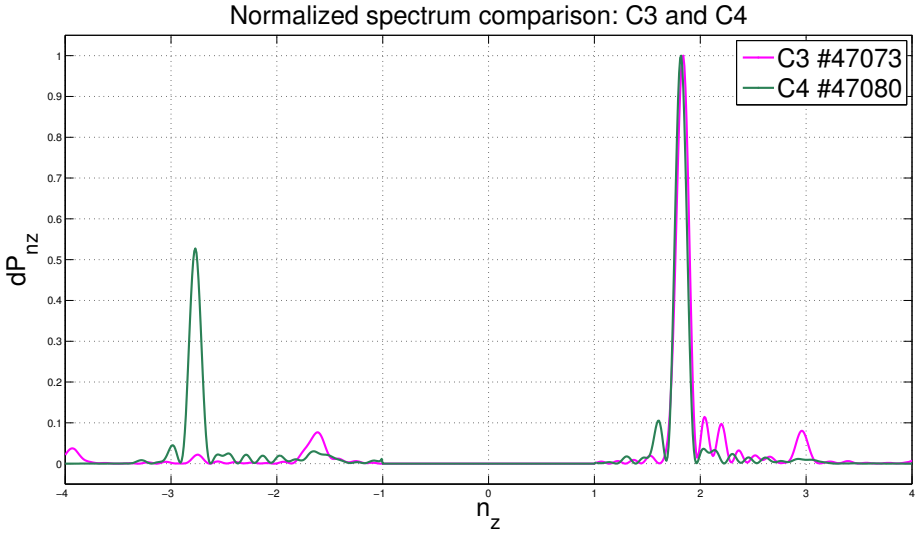

Figure 4.2: Comparison of typical C4 and C3 spectra. Note the presence of a significant negative peak in the C4 spectrum.

In ALOHA the coupled spectrum is calculated by treating the plasma as an antenna load. The coupled LH spectrum is used as input for the C3PO raytracing code, with the power rescaled with experimental measurement of the net incoming power ($P_{launched} - P_{refl}$).

As described in section 1.3.2, the main lobe in the spectrum located at the $n_{\|0}$ value, can be tuned in the phased array of the grill by changing the relative phasing between two adjacent modules ($\delta\Phi$). Power spectra are generated specifically for each discharge and as long as the launcher settings (power and phasing) and plasma edge conditions are the same, we do not need to compute new spectra for each time value of the discharge.

In discharge #45525, a scenario for which the current was driven by the C4 launcher, $n_{\|}$ of 1.72 and 1.82 in the two time intervals, thus two different spectra are used (one for 10-20 s with $n_{\|0} = 1.72$ and one for 20-34 s with $n_{\|0} = 1.82$). Figure 4.3 shows the spectra for the two different module phasing.

4.1.1 Upper and lower half launcher

Incident power from the klystrons is divided in the junction into upper and lower part of the launcher. Ideally the power is split equally into top and bottom part. The RF measurements used as input in ALOHA have an intrinsic uncertainty of at least

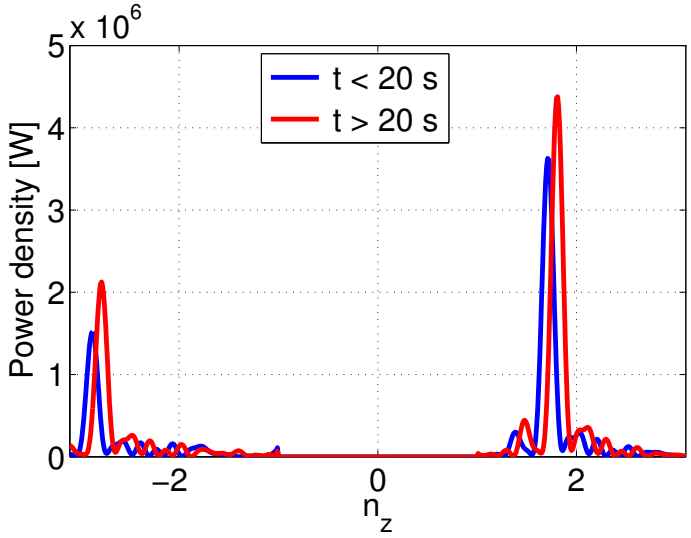

Figure 4.3: The two spectra used as input for the current drive simulations of discharge #45525. At $t = 20\,\mathrm{s}$ the phasing of the grill changes, corresponding to an increase of the $n_{\|0}$ which results in less efficient current drive, hence the power increase.

$\pm 5\%$, resulting in slightly different spectra for the two half launchers. The difference comes from the measurement of experimental power and phase of the launcher modules. There is also a small difference in the scattering matrices that describe the LH coupling between modules, which comes from the inherent numerical error of the RF software for calculating the matrices (HFSS) [9]. Therefore spectra from upper and lower module will be used in each simulation, depending on the launching position. Figure 4.4 shows a comparison of spectra from upper and lower launcher modules of C4.

4.1.2 Number of lobes in $n_{\|}$ spectrum

To minimize the computation time for the ray tracing and power absorption in C3PO/LUKE, the input spectrum that describes the coupled LH waves is a simplified version of the full ALOHA spectrum. The detailed ALOHA spectrum is decomposed into the a certain number of main lobes. The number of lobes with protected height and $n_{\|}$ location is specified by the user, with priority to the highest peaks. Clearly the more lobes are taken into account the more realistic the simulation is, but the contribution to current drive of lobes with low power or high parallel refraction index is low.

Each considered peak is fitted to an adjusted Gaussian function after power from surrounding peaks have been added. The height and central position in $n_{\|}$ space is unchanged, resulting in increased width of each selected lobe. In this way the total

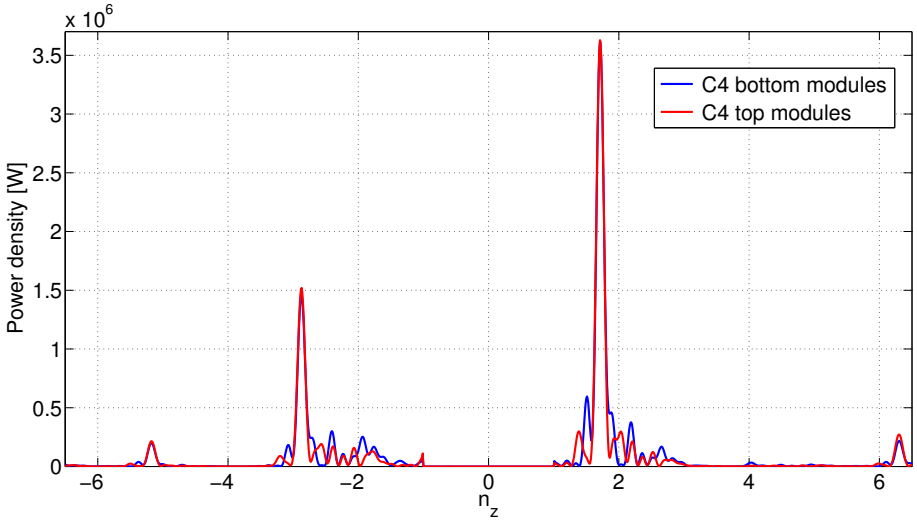

Figure 4.4: Spectra from upper and lower modules of C4 in discharge #45525.

power is conserved, but redistributed over the selected lobes resulting in a modified $n_{\|}$ distribution. The effect of the ignored lobes depends on the significance of the lobes, in terms of power, $n_{\|}$ value and synergetic effects with other lobes.

The number of selected lobes have been varied in simulations to reach convergence for the absolute plasma current, which occurs around six lobes for both C4 and C3 launcher. Since the results from only *two lobes* are generally near the converged results, such scenarios could be used as fast simulations which would be less reliable but useful for quick parameter scans. This systematic parameter scan is done for specified spectra for upper and lower half launcher. The total current is plotted and compared to simulations from upper launcher spectra in Figure 4.5 which shows the total driven current as a function of number of lobes in the spectrum from the C4 launcher.

Simulations were also done, where after the six lobes had been extracted and normalized, the number of lobes can be selected again but without power normalization and redistribution of $n_{\|}$. For discharge #45525 the result of four preserved lobes out of the six normalized gave very similar result in profile and absolute current to the standard case of redistributing all the power into six main lobes. On the other hand, if we redistribute the power into only four main lobes, the result differs noticeably from the convergent value of the total current (which occurs for six lobes). This means that the fifth and six lobes carry significant power but at higher $n_{\|}$ values, for which current drive efficiency is low.

4.1.3 Number of vertical launching positions

This parameter specifies the number of launched waves, and distributes them poloidally along the launcher. This is equivalent to discretizing the wave in the poloidal direction, whereas in reality the wave is continuous also in the poloidal direction. The waves are

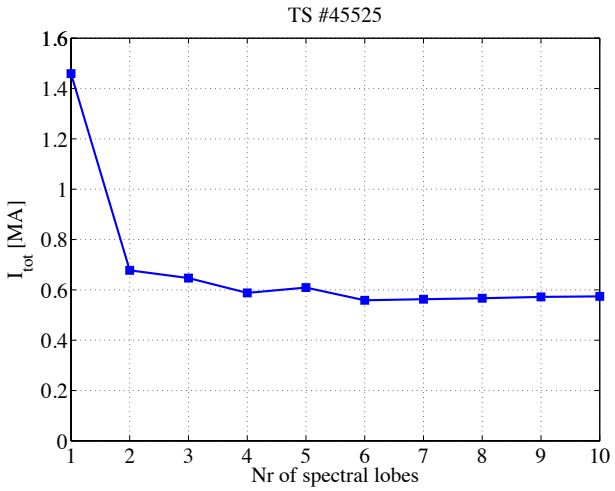

Figure 4.5: Current dependence on number of selected lobes from the detailed coupled LH spectrum for the discharge #45525 at 12 seconds. Six vertical launching positions are used. A clear convergence in total plasma current for six spectral lobes is observed.

launched from the upper or lower part of the counterlauncher with the corresponding reduced ALOHA spectrum. The scan of this parameter was performed with reduced ALOHA-spectra for two, four and six number of lobes. There is a clear convergence at 6 vertical launching positions and divergence at one single launching position, see Figure 4.6.

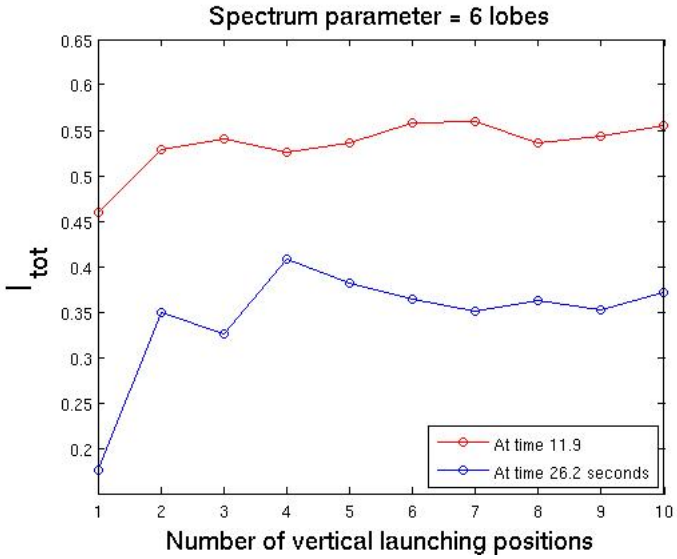

Figure 4.6: Current dependence on number of vertical launching positions.

4.2 Ray tracing

Plasma density and temperature profiles for discharge #45525, used as input in the LH simulations, are generated by METIS are shown in Figure 4.7.

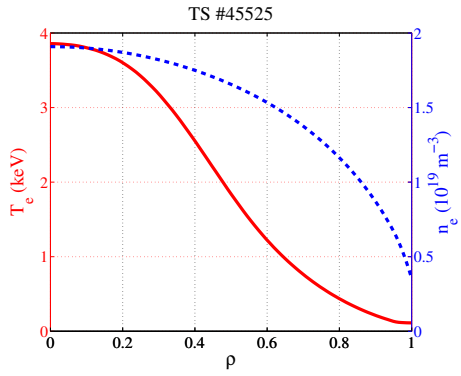

Figure 4.7: Density and temperature radial profiles, obtained by METIS for discharge #45525.

The C3PO ray-tracing calculations show that each of the 36 rays are all in the single or few pass regime for the #45525 discharge. The secondary lobe penetrates easily into the plasma and is absorbed in the center of the plasma where it efficiently drives a counter current. The main lobe, which drives a co current, is absorbed slightly off axis after a few passes, see Figure 4.8(a). Figure 4.8(b) shows the power absorption of the main and secondary lobe.

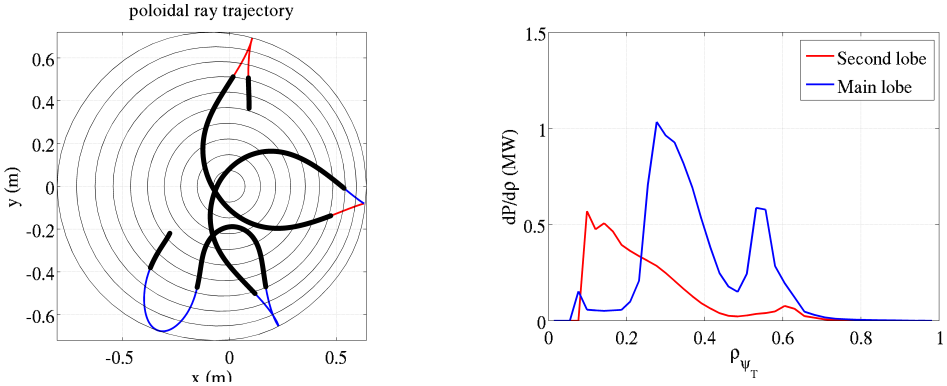

(a) Ray propagation of the main peak (blue) and the secondary (red) in the poloidal cross section of Tore Supra. Black lines show where the power absorption occurs.

(b) Power absorption of main (blue) and secondary (red) lobe, launched at $n_{\|} = 1.8$ and $n_{\|} = -2.78$.

Figure 4.8: Ray propagation (main lobe) and absorption (main and secondary lobe) from #45525 at $t = 27$ seconds.

4.3 HXR signal reconstruction

A synthetic diagnostic for the HXR emission detection from the suprathermal electrons is performed with the R5X2 code. Excellent agreement of of the reconstructed bremsstrahlung emission with the detector count rate is found, in both absolute amplitude and profile shape.The main difference in the comparison is the hollow profile in the central chords. This feature decays with the invoking of a uniform radial diffusion coefficient D_r $[m^2/s]$. An energy independent diffusion coefficient for the fast electrons, which is typical for electrostatic turbulence, is motivated by the shape of experimental HXR profiles that do not vary with the photon energy, see Figure 4.9.

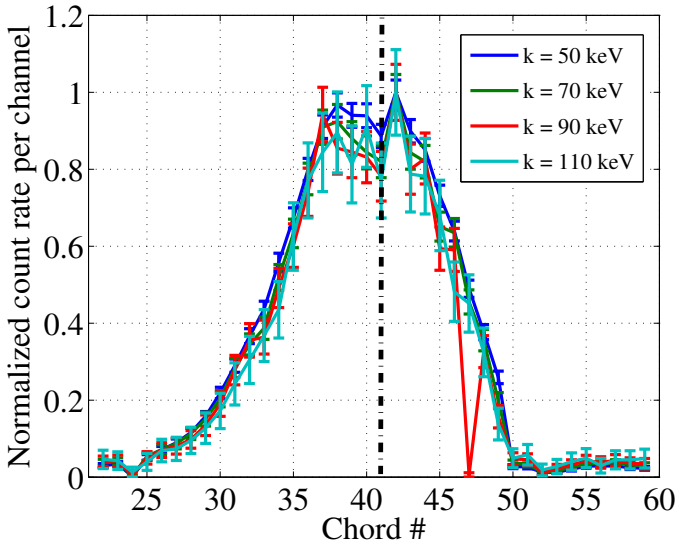

Figure 4.9: Normalized count rate measured in various energy channels for discharge #31527.

Figure 4.10(a) shows the total count rate in the range $50-110\,\mathrm{keV}$ for different values of the diffusion coefficient (D_r). The simulated radial profile and photon temperature and count rate for different D_r values is shown in Figure 4.10(b) and 4.10(c). The comparison of HXR measurement and simulation results shows good agreement for $D_r = 0.1\,\mathrm{m}^2/\mathrm{s}$ in the energy range $60 < E < 80\,\mathrm{keV}$.

The simulated photon temperature agrees well with the experimental observations, see Figure 4.11. The agreement holds through the pulse, the count rate in the central line of sight as a function of time is shown in Figure 4.12.

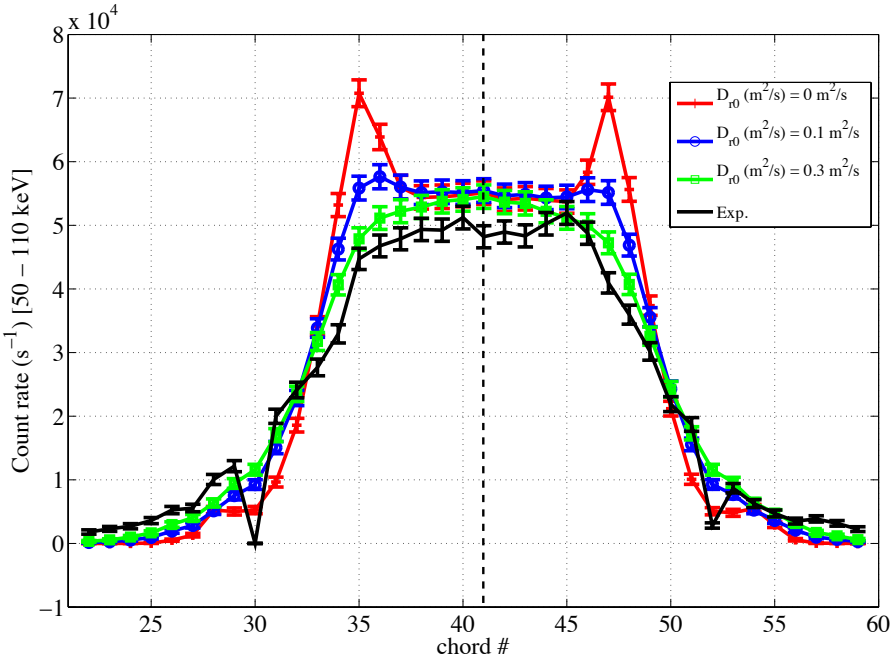

(a) Comparison of the total count rate in the range 50-110 keV with simulations for different D_r values shows that simulation with D = 0.1 m^2/s results in excellent agreement with the experimental profile.

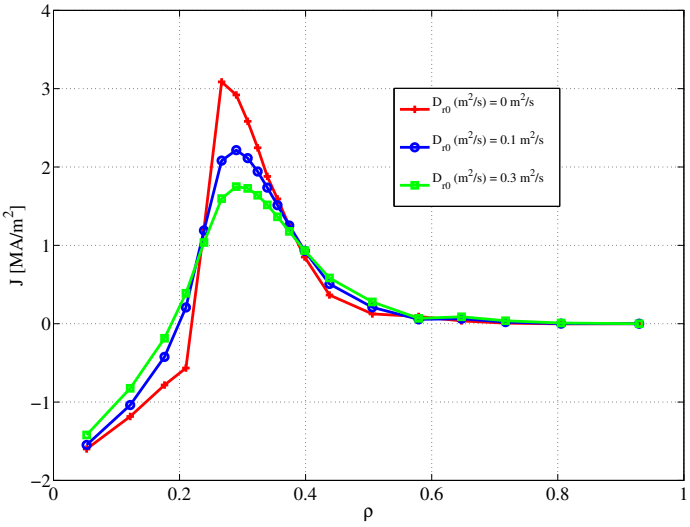

(b) Simulated radial current profile for different D_r values.

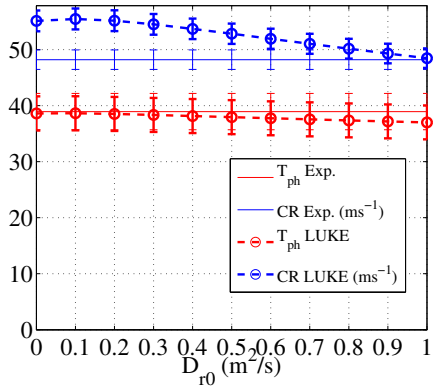

(c) Photon temperature and count rate as a function of D_r.

Figure 4.10: Simulation results including the effect of radial diffusion compared to experimental measurements, for pulse #45525 at $t = 27$ seconds.

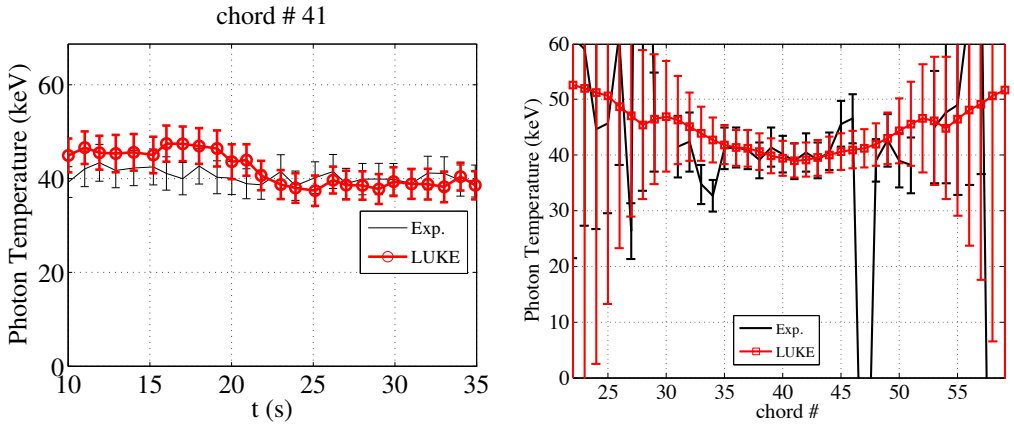

(a) Photon temperature evolution in the central chord.

(b) Photon temperature as a function of chord number, at 28 seconds.

Figure 4.11: Simulated photon temperature compared to experimental measurements, for pulse #45525.

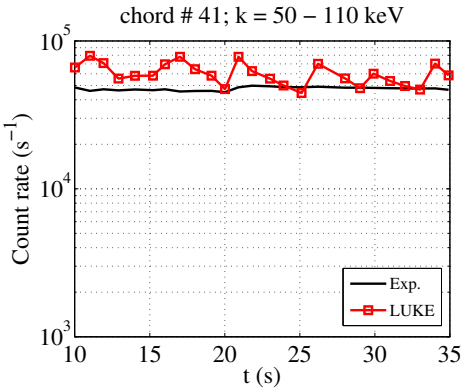

Figure 4.12: Total calculated count rate in the central line of sight in the energy range 50-110 keV for #45525.

4.4 LH current

LUKE simulations are performed for $6 \times 6 = 36$ rays for each second through the discharge. Over the period where same spectrum is used, only the equilibrium conditions (magnetic equilibrium profile, plasma density profile and electron temperature) vary. In Figure 4.13(a) the total toroidal plasma current, experimental and LUKE computed, is presented. Since this is a full current drive scenario the Ohmic current contribution is negligible. The experimental current consists of the LH driven current (I_{LH}) and bootstrap current (in Tore Supra usually around 10 % of the total plasma current I_p). In association with a multi junction module phase shift at $t = 20$ seconds, the current drops slightly even though the LH power increased. The relative drop is larger in the

simulations than the experimental results show.

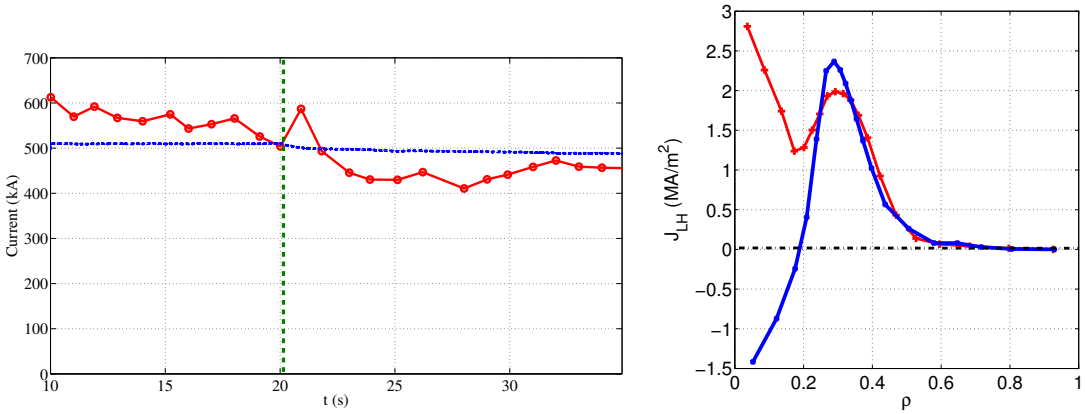

(a) Total toroidal plasma current simulated by LUKE for discharge #45525 compared to experimentally measured current.

(b) Radial current profile for 12 s (red) and 27 s (blue).

Figure 4.13: Simulated LH current for discharge #45525. At $t = 20$ seconds, the current drops slightly due to an increased main $n_{\|}$ even though the LH power was increased.

Figure 4.13(b) shows the radial current profile. The negative driven current in the plasma center for the second time interval of the pulse is driven by the secondary lobe in the spectrum, at $n_{\|0} = -2.78$. Since this is a radial profile, the impact on the total current increases with ρ^2 (where $\rho = r/a$ is the normalized minor radius of the tokamak), which means that the contribution to the total current is smaller than current driven more off-axis, but the central profile is still very important for plasma stability and confinement.

4.5 Interpretation of the HXR signals

The raw HXR signal consists of count rate as a function of a chord number, with a line of sight cutting through the poloidal cross section as seen in Figure 2.5. Abel inversion, practical for projection of axially symmetric functions onto a plane, of HXR measurement in the energy range $60 < E < 80$ keV as a method of measuring the current profile has routinely been used over the years for currents driven by the C3 launcher in Tore Supra. The method has not yet been validated for C4.

For the shot #45525, which is a low density ($n_e = 1.4 \times 10^{19}\,\mathrm{m}^{-3}$) and high temperature ($T_0 = 3.7$ keV) discharge, ray-tracing with C3PO show that the rays are absorbed after one or a few passes and therefore are considered to be within the validity range. The simulations show that the secondary lobe that drives the negative current easily penetrates into the plasma and is absorbed in the center of the plasma. The main lobe drives a positive current and is generally absorbed more off axis.

The simulated HXR bremsstrahlung emission compares well to experimental mea-

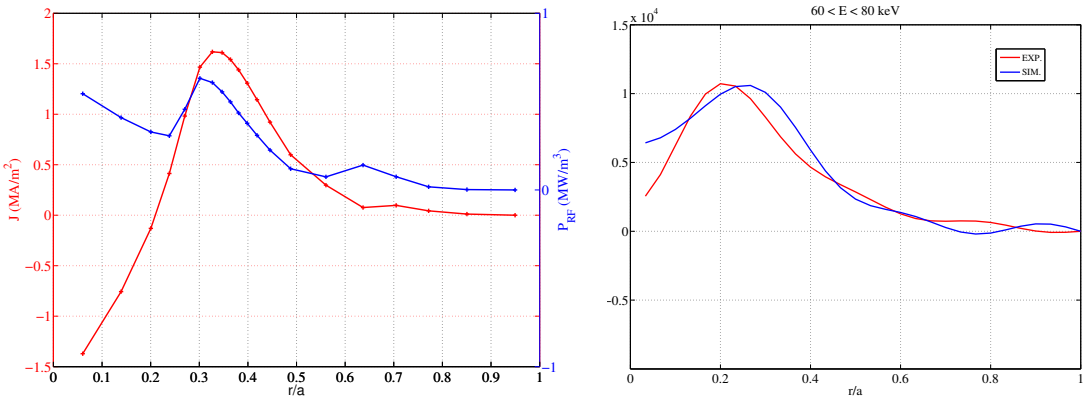

(a) (b)

Figure 4.14: Discharge #45525, C4 launcher drives the LH current. (a) Current and power deposition profile obtained by C3PO/LUKE simulation. (b) Abel inverted Bremsstrahlung emission profile of HXR signal measurement compared with R5X2 simulation.

surements, see Figure 4.14(b). However, it is important to notice that the current profile calculated by C3PO/LUKE is different to the Abel inverted profile, see Figure 4.14(a). Inversion of the simulated HXR emission of the C3 launcher, on the other hand, works better as an estimate of the current profile. This is exemplified by a simulation of discharge #31527 where the LH current was driven by the C3 launcher, i.e. a FAM launcher. See Figure 4.15 where C3PO/LUKE simulated current profile and inverted HXR profile is compared with the inverted experimental HXR emission. In this case at least the peak of the LUKE current profile agree with the inverted FEB measurement.

Abel inverted HXR emission, synthetically reconstructed with the simulation code R5X2 agrees well with the inverted experimentally measured HXR emission. Even though the bremsstrahlung emission is a powerful diagnostic tool that provides an insight in the physics of LH generated fast electrons, it is not possible to recreate the electron distribution function from the HXR data. It is clear that this profile differs from the simulated radial current profile. This is explained by the fact that HXR signal, a count rate, is a positive measurement and does not contain information about the direction of the emitting electrons. If there is current driven in opposite directions, interpreting the inverted HXR data as a measurement of toroidal current profile is inaccurate. Two identical LH beams launched in opposite toroidal directions would generate zero net current but a considerable HXR emission. Thus, HXR profile only gives information about the power absorption and not about the net current.

Inverted HXR profiles can be used as a relative measurement of the driven current *if* the contribution from counter current driving rays is negligible. Thus it is misleading to analyze a reconstructed Abel inverted profile when there is both positive and negative current components present. This is the case for the C4 launcher, that in the LH spectrum apart from the main lobe has a significant secondary lobe at a relatively low

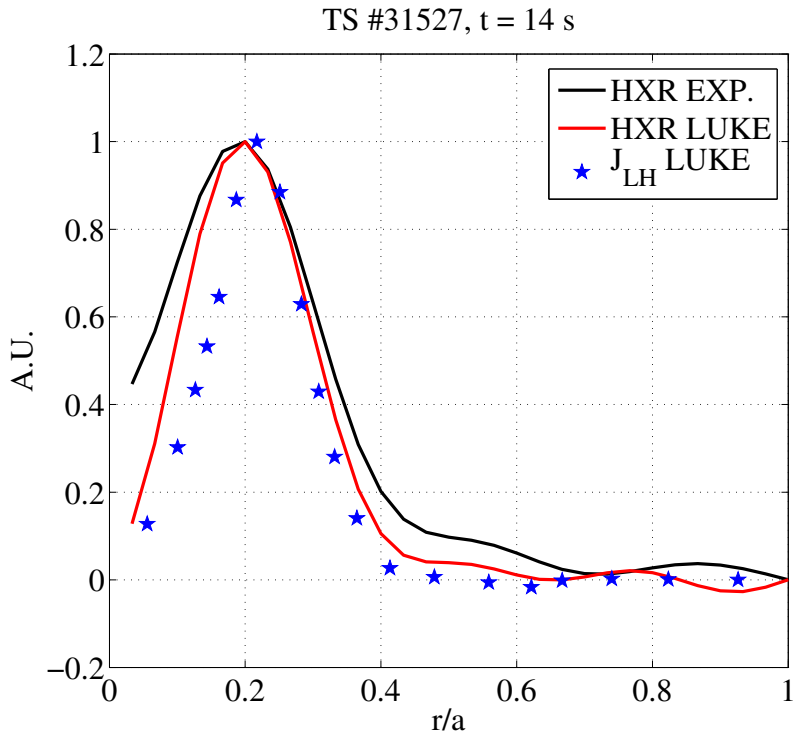

Figure 4.15: Comparison of simulated HXR count rate and experimental measurements of discharge #31527 where the LH wave was provided the FAM C3 launcher. The HXR inverted profiles, both experimentally measured and reconstructed with R5X2 compares fairly well to the C3PO/LUKE computed current profile.

$|n_{\parallel}|$ that drives a current in opposite direction. A significant counter current driving lobe is a consequence of the design that includes passive waveguides between the active ones. It is therefore misleading to compare FAM and PAM bremsstrahlung emission, as a measurement of current drive efficiency in similar scenarios.

4.6 Internal inductance

The internal inductance (L_i) of the plasma can be used as a parameter to assess the quality of a simulation in METIS. It is related to the current profile. If the simulated L_i agrees with measurements, the modelling of the equilibrium is considered to be satisfactory. The METIS simulation routine is to use the current average deposition (ρ) and profile width ($d\rho$) to describe the current profile. We have shown that the inverted HXR signal is not comparable with the LUKE calculated current profile. By defining the current profile by the parameters given by LUKE in discharge #45525, an L_i closer

to experimental measurements is obtained, see Figure 4.16. This demonstrates the difference between inverted HXR signal and the current profile, but also suggests that the LUKE current profile gives a more realistic description of the current profile than the inverted HXR signal.

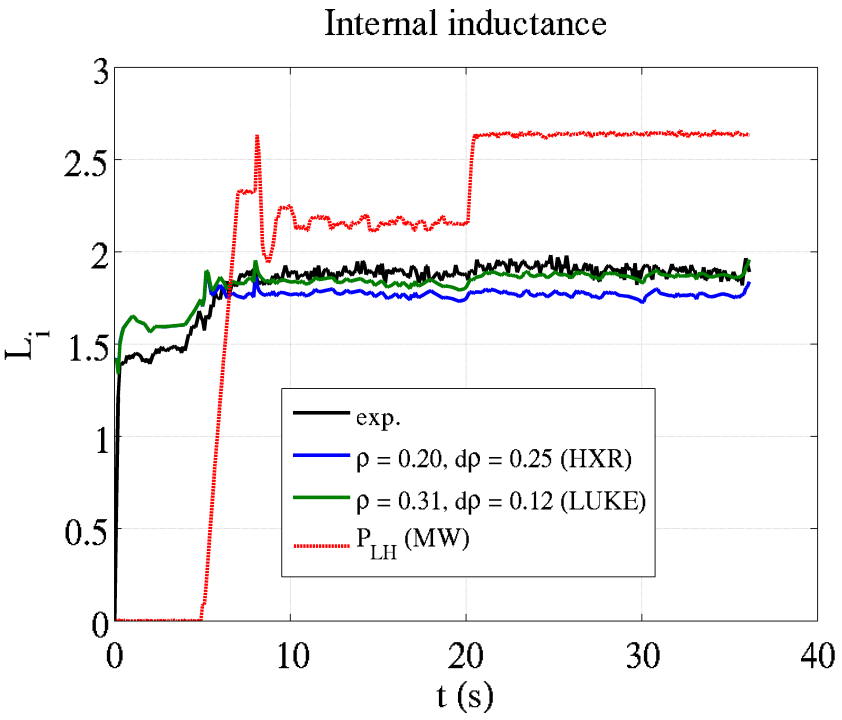

Figure 4.16: The internal inductance (L_i) from METIS simulation agrees better with measurements with LUKE current as input than inverted HXR signal.

4.7 Summary

The number of vertical launching positions have shown clear convergence for the total plasma current at 6 vertical launching positions and 6 lobes from the power spectra. This gives a total of $6 \times 6 = 36$ rays for each simulation. The same optimization process was performed for the C3 launcher, resulting in the same choice of simulation parameters for the launched LH wave.

In this chapter, the simulation process was demonstrated for the full current drive discharge #45525 and parameter optimization with the C4 launcher was presented. Good agreement was found in the reconstruction of the HXR signal, both in shape and absolute amplitude. Also the simulated current agrees well with the measured plasma current.

5

Application to Tore Supra

To demonstrate the capacity of the LHCD calculations for a C4 driven scenario the full simulation procedure was presented in the previous chapter. A number of discharges have been performed in Tore Supra, using either one or both launchers, in a variety of plasma conditions including fully non-inductive scenarios. In this chapter a more general overview is given by presenting results from the following types of modelled scenarios:

- Full current drive scenarios: Current driven completely by either C3 or C4, with $V_{loop} = 0$.
- Current driven by both C3 *and* C4 simultaneously. Synergetic effects are assessed.

The results are compared to experimental measurements and the effect of the spectral properties of different launcher types and settings is addressed. Plasma and launcher parameters for each simulated scenario, used as simulation input, are presented in Appendix A where Table A.1 provides an overview of the different types of modelled scenarios.

5.1 Comparison of launcher design

As discussed in previous chapter, the conceptual properties in launcher design result in different current drive properties. In this section the effect of the spectral properties will be assessed by comparing similar scenarios driven by *either* C3 or C4. First, a full current drive scenario with the C3 launcher (#31527) is analyzed and the experimental agreement is compared to the result of the #45525 discharge that was presented in the Chapter 4.

5.1.1 Full current drive

The LUKE/C3PO calculated current profile and current drive efficiency for the C4 driven full current drive scenario #45525 was thoroughly presented in the previous chapter.

A *C3 driven* full current drive case was also modelled. Just like the C4 driven scenario (#45525), #31527 is driven in fully non-inductive condition. Measured LH power, density, plasma current and loop voltage is presented in Figure 5.1. The phasing between the waveguide modules, which was held constant during the discharge, was such that the main parallel refractive index was 1.72.

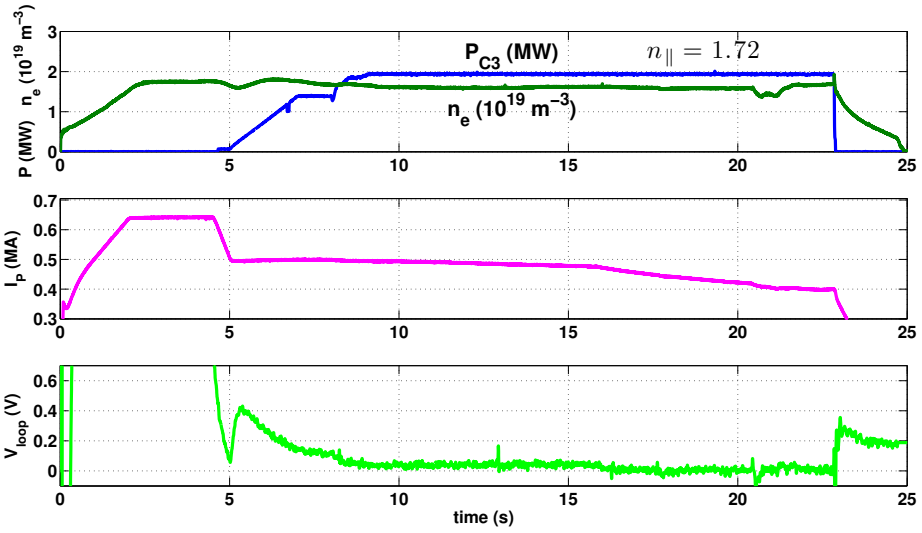

Figure 5.1: Data from discharge #31527.

Also for this discharge, the reconstructed FEB emission agrees very well with the experimental measurement when a small radial diffusion ($D_r = 0.1\,\mathrm{m}^2/\mathrm{s}$) coefficient was invoked. See Figure 5.2(b).

The photon temperature is overestimated by LUKE, see Figure 5.3. In both C3 and C4 modelling the HXR emission count rate agrees well with experimental measurements, both in shape and absolute count rate. The photon temperature is overestimated for the C3 scenario, but for C4 it is very well modelled. The main difference between the C3 and C4 modelling is the total plasma current, which in these cases of full current drive consists of only the LH current. For C3 driven scenarios the plasma current is overestimated in LUKE, see Figure 5.4. This is a general pattern in the simulations with C3 and C4, which we will come back to in Section 5.3.

5.2 Both launchers

Discharges where C3 and C4 launchers simultaneously provided the LH power have been modelled. Two consecutive pulses under the same plasma density and similar LH power from C3 ($P_{LH} = 3.0\,\mathrm{MW}$) and C4 ($P_{LH} = 2.4\,\mathrm{MW}$) were performed. The two launchers were used simultaneously to drive the LH current of totally ($P_{LH} = 5.4\,\mathrm{MW}$).

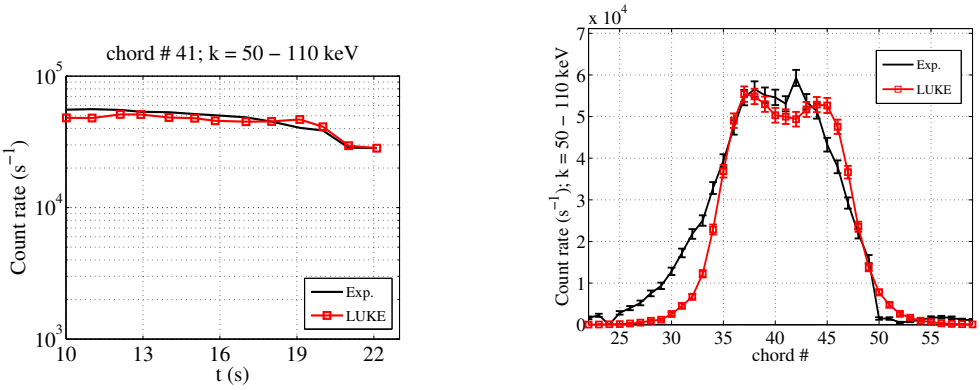

(a) Count rate in the central chord as a function of time.

(b) The count rate in each chord at 14 seconds.

Figure 5.2: Reconstructed FEB emission from C3 driven current in discharge #31527 compared with measurements.

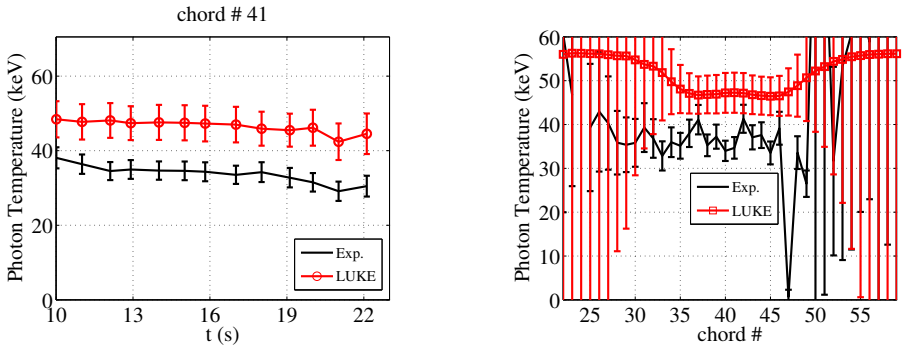

(a)

(b)

Figure 5.3: Photon temperature from the reconstructed HXR signal compared to measurements.

The difference between the pulses is that one of the klystrons that feed the C4 launcher was incorrectly phased in the #47955, which was corrected for in #47957. In the case with the klystron error, the current drive efficiency is found to be lower than in the corrected case. Since all the conditions where the same in the two discharges, the difference must arise from the klystron error. In order to asses the spectral effects, the two scenarios are simulated in C3PO/LUKE with ALOHA generated power spectra.

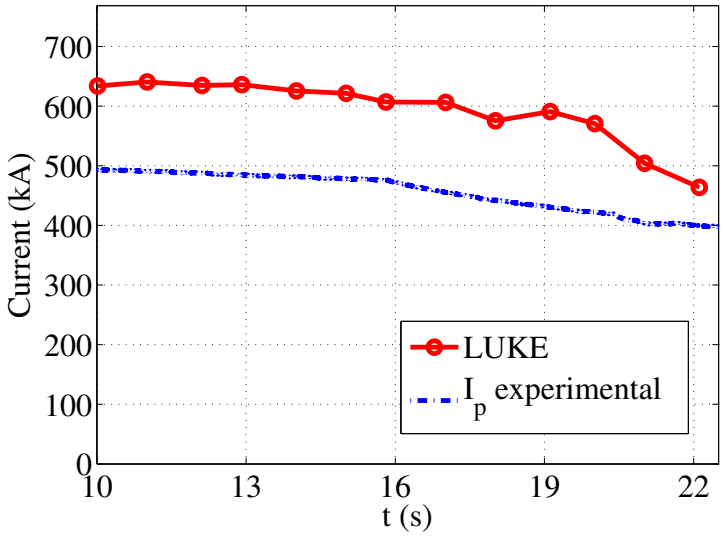

Figure 5.4: Total toroidal plasma current simulated by LUKE for discharge #31527 compared to experimentally measured current.

Table 5.1: LHCD calculation results for each scenario.

Discharge	P_{abs}[MW]	$I_{LH}(LUKE)$[kA]	η_{LH}	$I_{exp}(I_{LH}+I_{boot})$	η_{exp}
#31527	1.95	590	0.154	430	0.101
#45525 ($t = 11$ s)	2.1	575	0.0887	508	0.0705
#45525 ($t = 26$ s)	2.6	447	0.0560	494	0.0562

5.2.1 Effect of phasing error

The relative phasing of the klystrons and consequently between neighboring waveguides in the grill was supposed to be 180 ° phase shift, but in #47955 the sixth (out of eight) klystron had approximately the same phase as its neighbors. To see if the reduction of current drive efficiency in #47955 compared to #47957 was caused by the spectral difference due to incorrect tune of the sixth klystron, ALOHA coupled spectra were generated to simulate the two pulses. To capture the impact of the spectral effects, the same magnetic field, temperature and density profile were used for both discharges in the current drive modelling. This approximation is acceptable since the plasma properties were similar for both cases.

The ALOHA generated spectra of the C3 and C4 launchers from pulse #47957 are seen in Figure 5.5. The spectra look like typical C3 and C4 spectra and the main lobes initial parallel refractive indices are respectively 1.9 and 1.7.

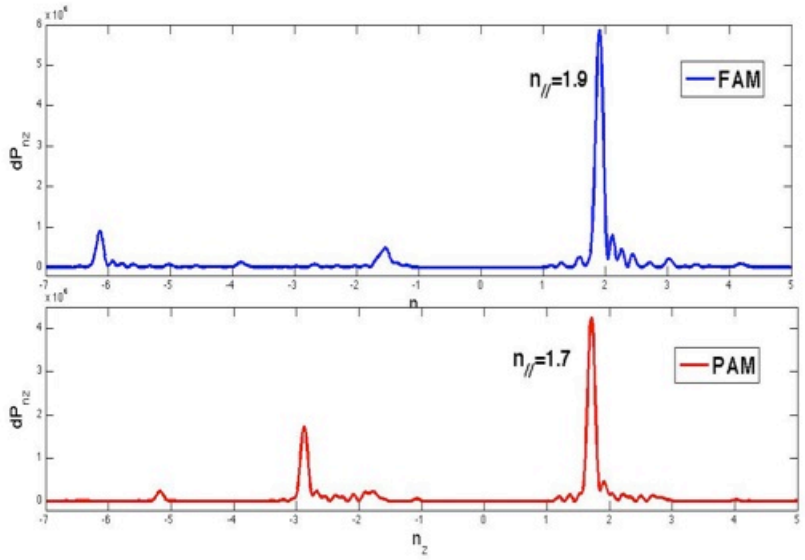

Figure 5.5: ALOHA generated spectra for C3 and C4 in pulse #47957.

As expected, the spectrum for the C3 launcher is identical to the #47957 discharge. The calculated ALOHA C4 spectrum in the #47955 (Figure 5.6), on the other hand, is different from the traditional C4 spectrum, compare with Figure 5.5. The main peak is slightly shifted to $n_{\|} = 1.73$ compared to in #47957 where the main lobe was at $n_{\|} = 1.71$. The spectrum is distorted and the power is distributed in so that the power of the main peak is reduced compared to the design case, where no phase error was present in the sixth klystron.

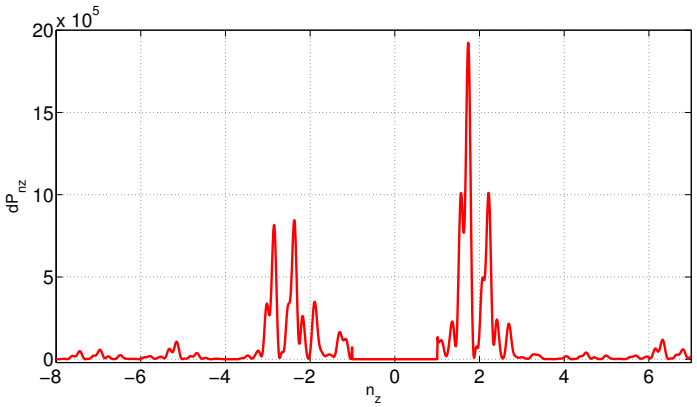

Figure 5.6: An omitted phase shift between two of the klystrons results in a distorted spectrum. ALOHA generated spectra for C4 in pulse #47955.

That a similar spectrum to the #47957 case is obtained in ALOHA when manually

correcting the phase of the detuned waveguide, is a clear indication that the spectral properties change considerably if one klystron is set out of phase. By manipulating the input phase in ALOHA simulations in the C4 waveguide array, we conclude that the distortion is stronger when a waveguide with neighbors is out of phase, than for a detuned waveguide on the edge of the array. This is not surprising, since the drivers in the center can cross-couple more to the other waveguides through the edge plasma than an active waveguide on the edge of a row.

The phasing error results in several additional peaks and decreased directivity with a power spectrum that is more symmetric around $n_z = 0$ than for a correctly phased C4 array.

Figure 5.7 illustrates the modelled power absorption and current profile for the two pulses. Even though the power deposition is similar for the two scenarios, the resulting net current is smaller for discharge #47955. The C4 driven current we saw in #47957 at $\rho = 0.3$ is almost non existent in #47955. This means that the LH power deposited here give rise to equal parts of co and counter driving current. The change in C4 waveguide phasing results in smaller driven current than in #47957, even though the input LH power is the same. In other words, the #47955 scenario is less efficient than #47957 due to spectral effects of the launched C4 spectra. Due to the phasing anomaly the computed current drive efficiency is $0.1162\,\mathrm{A/W/m^2}$ compared to $0.1302\,\mathrm{A/W/m^2}$ in discharge #47957. This difference does not seem that large, but let us into the separate current drive contributions of the both launchers. Simulating the C3 launcher drives similar current for the two discharges, with a $\eta = 0.1384\,\mathrm{A/W/m^2}$ and a current of 0.49 MA. The simulation results from C4, on the other hand, differs significantly between the two discharges. The plasma current of #47955 is 0.146 MA and $\eta = 0.05735\,\mathrm{A/W/m^2}$, compared to #47957 ($I_p = 0.2629\,\mathrm{MA}$ and $\eta = 0.1089\,\mathrm{A/W/m^2}$). For the total plasma current, the phasing error results in a current that is only 89 % of the ideal case value.

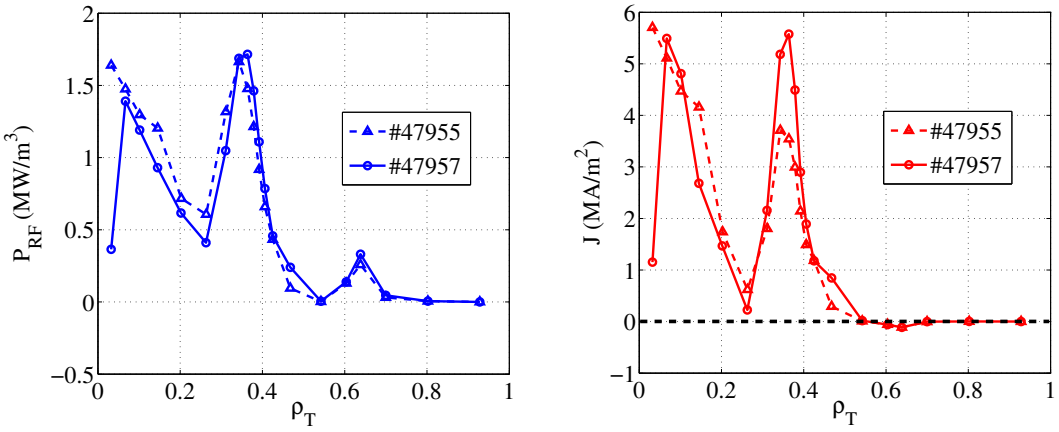

Figure 5.7: Total absorbed LH power and net current profile #47955 and #47957 when driving current with C3 ($P_{LH} = 3.0\,\mathrm{MW}$) and C4 ($P_{LH} = 2.4\,\mathrm{MW}$) launchers simultaneously.

5.2.2 Synergy effect

Since the effect a single spectral lobe in the LH spectrum has on the plasma, depends on the electron distribution function, which is constantly under the influence of the LH power, there will be a synergetic effect between the lobes in a spectrum. In the pulses, like #47957 where two launchers where in used with *different* main parallel refractive index ($n_{\|C3} = 1.9$ and $n_{\|C4} = 1.7$), a synergetic effect between the spectral lobes of each launcher can be expected.

To understand how the effect of the LH waves from the C3 and C4 couple, the entire scenario was simulated with only C3 or C4, using the same profiles but *only one* launcher.

The sum of the total current of the simulation using only C3 or C4 do not add up to the conventional #47957 scenario where both C3 and C4 were involved. This implies synergy between the waves from the two launchers. The separate contribution to the calculated current is 0.494 MA from C3 and 0.263 MA from C4. These two separate contributions do not add up to the total simulated current $I_{LH} = 0.0.825$ MA. In this case, the synergetic effect contribute to about 8 % of the total plasma current.

5.3 Overview of full current drive scenarios

In Figure 5.8 the computed current drive efficiency from the *full* current drive simulations is compared to the experimental current drive efficiency according to Equation 1.5. The standard major radius for Tore Supra ($R = 2.38$ m) and density (n_{20}) and LH power (P_{LH}) according to Table A.1. Since these were full current drive cases ($V_{loop} < 50$ mV) the ohmic current is considered negligible. Thus, the plasma current in these cases consist of the LH current and about 10% bootstrap current. The LH current is therefore assumed to be 90% of the measured plasma current and a bootstrap fraction of 10% is subtracted from the measured plasma current.

The simulated plasma current agrees with experimental measurements for discharges with C4 driven current. Simulations of C2 and C3 discharges seem to systematically result in a LH current about two times the experimental current. The severe overestimation of discharge #32299 could be explained by the presence of MHD instabilities that was observed during the experiment, where the aim was to drive a current of 1 MA. The observed MHD modes could be the reason why the plasma current was lower than expected.

5.4 Sensitivity to edge density

The edge density uncertainty constitutes a major error in the current drive calculations. To investigate whether this might be behind the generally overestimated plasma current of C3 calculations, LHCD calculations were performed with LH spectra of different possible edge densities. The Langmuir probe data for discharge #31527 measured $4 \cdot 10^{17}\,\mathrm{m}^{-3}$, which is what we use in the previous #31527 results. According to the model

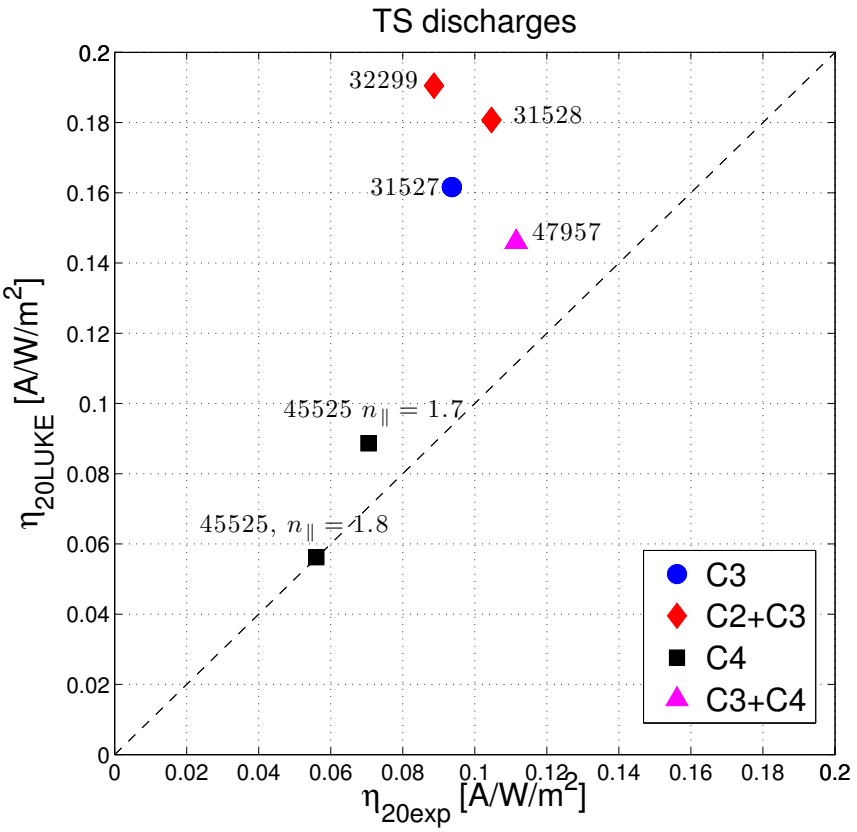

Figure 5.8: C3PO/LUKE calculated current drive efficiency compared to current drive efficiency from experimental plasma current measurements (the assumed 10% bootstrap current is subtracted from the measured plasma current).

in Section 2.2.2 the actual edge density at the launcher mouth can be assumed to be between $\frac{4}{e} \cdot 10^{17} = 1.5 \cdot 10^{17}$ and $4 \cdot 10^{17}\,\mathrm{m}^{-3}$.

Another approximation of the edge density was done by using the edge density for which ALOHA gives the same reflection coefficient (RC) as experimental measurements. For this pulse measurements indicated $RC = 5\%$, which in ALOHA corresponds to edge density of $1.25 \cdot 10^{17}\,\mathrm{m}^{-3}$. C3PO/LUKE calculations with spectra defined for the three different densities, show that the directivity ($P_{codriving}/P_{tot}$) and the LH current increase with the edge density, see Table 5.2. Calculations with spectra generated with $n_e = 1.5 \cdot 10^{17}\,\mathrm{m}^{-3}$ gives absolute current very close to the experimental plasma current for the full current drive case #31527. The directivity was also changed manually by selecting the most powerful lobe from the ALOHA spectrum in each toroidal direction ($n_\parallel = [1.72, -1.73]$) with widths $dn_\parallel = [0.0821, 0.1110]$ and varying the directivity from $50 - 100\%$. The current increases with the directivity and consequently with the edge density, see Figure 5.9. This shows that calculations are very sensitive to the edge density

Table 5.2: ALOHA result for different density, discharge #31527.

Edge density (m^{-3})	RC (%)	Directivity	$n_{\|\|}$ weighted directivity	I_{LUKE} $[MA]$
$1.25 \cdot 10^{17}$	5	0.67	0.32	0.42
$1.5 \cdot 10^{17}$	3	0.70	0.37	0.44
$4 \cdot 10^{17}$	2	0.74	0.48	0.62

in the edge density regime typical for Tore Supra discharges.

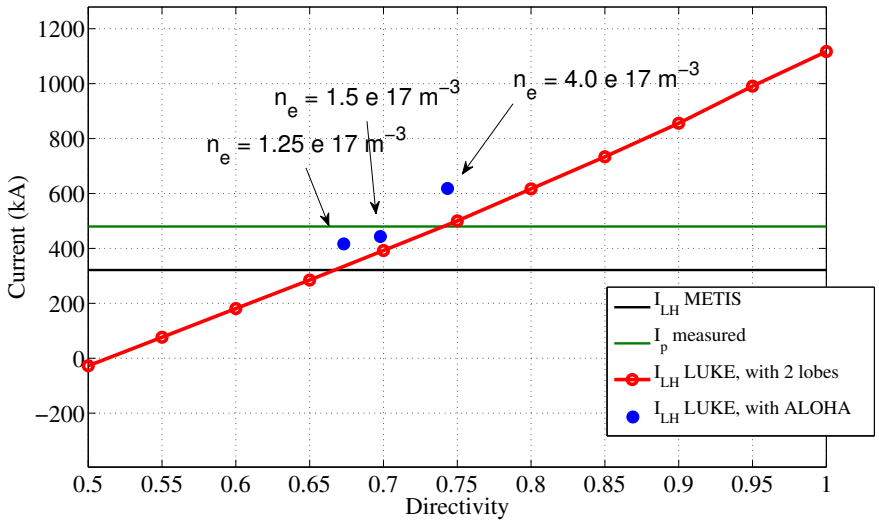

Figure 5.9: C3PO/LUKE calculated LH driven current as a function of directivity compared to the experimental plasma current ($I_{LH} + I_{bootstrap}$)

That the current is non-zero for equal power in positive and negative lobe is due to that the lobes have different width and are slightly different positioned, which causes an asymmetry and non-zero current at 50% directivity, see Figure 5.10(a). Even though the current increases with directivity the reconstructed HXR signal remains constant, see Figure 5.10(b). This supports the discussion from Section 4.5 about that the HXR signal can not be used as a measurement of the current profile.

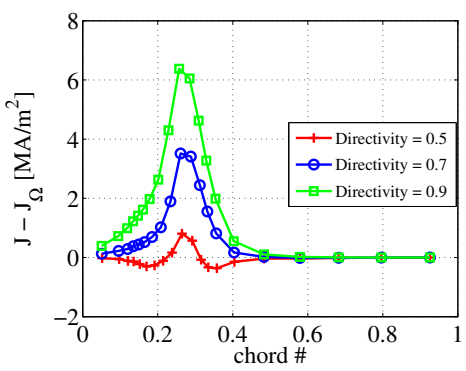

(a) Current profile for different directivity.

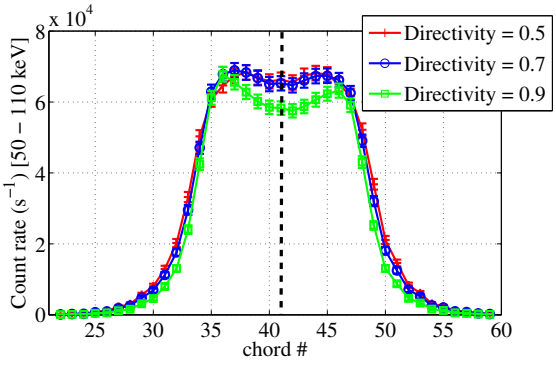

(b) Reconstructed HXR signal as a function of the chord of each HXR camera, from simulations with different directivity in LH spectrum.

Figure 5.10: Discharge #31527 driven with the two most significant lobes of C3 with varied directivity.

6

Conclusion and Outlook

The simulation suite C3PO/LUKE has been demonstrated for LH current driven with the Passive Active Multijunction (PAM) launcher (C4). This was done by systematically optimizing the simulation procedure aiming for fast simulation with a stable solution. Provided a detailed spectrum generated by the coupling code ALOHA it was found that 36 rays, corresponding to the six waveguide rows and the six main lobes in the LH spectrum, are sufficient for a satisfactory description the LH wave propagation. The electron distribution function is calculated by the 3D Fokker-Planck code LUKE. Full convergence is obtained in the self-consistent calculation of the distribution function and the power absorption along all rays. An excellent agreement with experimental observations, *both* in absolute amplitude and profile shape for the reconstructed HXR emission, gives confidence in the simulation suite for the new ITER relevant C4 antenna.

Comparison of C3 and C4 in full current drive scenarios shows that LUKE tends to overestimate C3 current. The shape of HXR signal is matched for both launchers. A possible explanation was given by assessing the sensitivity of directivity for the C3 launcher, and thereby the edge density model for ALOHA input.

METIS and CRONOS simulations use inverted HXR profiles, as a first estimate of the LHCD to be able to calculate current diffusion and provide C3PO/LUKE with an equilibrium. This approximation was validated for the C3 launcher and works well since the significance of the spectral negative lobes is small. Since the HXR detection system registers photon count rate and can not differ between co and counter driven electrons, the signal is a measurement of the power absorption rather than the driven current. For scenarios where the current is driven LH waves with significant negative lobes, the current deposition and power absorption profile are not necessarily the same. This means that the METIS/CRONOS calculated current profile is, at least in cases with C4, can be misleading and incorrect. Since these simulations are used to compute input data for LUKE such as loop voltage and magnetic field strength this error propagates in

the C3PO/LUKE simulations. METIS simulations showed better results when, rather than using the inverted HXR to describe the current profile, taking LUKE simulated current as input. This not only shows the difference between the two profiles, but also supports the LUKE current profile to be more realistic. The next step is to use the improved, LUKE current based METIS simulation as equilibrium input in LUKE and iterate between LUKE and METIS until convergence.

The negative lobe in the PAM spectra leads to a reduced driven current. Thus research for the future ITER LHCD launcher should aim at reducing the negative lobe.

The outcome of discharge #47955 was understood. C3PO/LUKE obtained current drive efficiency trends compare well with experimental results. The distorted spectral effects of C4, due to an out of phase klystron, was responsible for the decreased current drive efficiency. This shows that the simulation suite is sensitive to details in LH spectrum.

A case of current driven by both C3 *and* C4 simultaneously was modelled. Synergetic effects are assessed. According to the simulation it seems like there is *power to gain* if we use two launchers with different $n_{\parallel}$, as in the case of #47957. A substantial part of the plasma current comes from non-linear effect between the rays of two launchers.

To gain understanding in the directivity of the C3 launcher experiments could be performed where the edge density at the launcher could be varied or controlled. Difficulty lies in that the directivity and reflection coefficient is very sensitive for C3 around the cut off density. By driving LH current with edge density in a region where the directivity is less sensitive ($2 - 3$ times cut off density), it will be easier to approximate the edge density used for the ALOHA simulations.

This work could be continued by extending the simulation database of full current drive cases. It would be useful to in the next experimental campaign compare current drive efficiency on C3 and C4, in exactly the same plasma conditions in full current drive.

Bibliography

[1] Landau damping, Wikipedia, March 2012. URL http://en.wikipedia.org/wiki/File:Maxwell_dist_ress_partic_landau.svg.

[2] Fusion for energy, January 2011. URL fusionforenergy.europa.eu/understandingfusion/.

[3] T. Yamamoto. Experimental observation of the rf-driven current by the lower-hybrid wave in a tokamak. *Physical Review Letters*, 45(9):716–719, 1980. doi: 10.1103/PhysRevLett.45.716.

[4] S. Bernabei. Lower-hybrid current drive in the plt tokamak. *Phys. Rev. Lett.; Physical Review Letters*, 49(17):1255–1258, 1982. doi: 10.1103/PhysRevLett.49.1255.

[5] A. Ekedahl et al. Validation of the iter-relevant passive-active-multijunction lhcd launcher on long pulses in tore supra. *Nuclear Fusion*, 50(11):112002, 2010. URL http://stacks.iop.org/0029-5515/50/i=11/a=112002.

[6] G. Giruzzi. Measurement of the hot electrical conductivity in the pbx-m tokamak. *Nuclear Fusion*, 37(5):673–674, 1997.

[7] G.M Wallace et al. Absorption of lower hybrid waves in the scrape off layer of a diverted tokamak. *Phys. Plasmas*, 17(8):082508–082508–11, 2010. ISSN 10897674. doi: 10.1063/1.3465662.

[8] J.F. Artaud et al. The cronos suite of codes for integrated tokamak modelling. *Nuclear Fusion*, 50(4):043001, 2010. URL http://stacks.iop.org/0029-5515/50/i=4/a=043001.

[9] J. Hillairet, D. Voyer, A. Ekedahl, M. Goniche, M. Kazda, O. Meneghini, D. Milanesio, and M. Preynas. Aloha: an advanced lower hybrid antenna coupling code. *Nuclear Fusion*, 50(12):125010, 2010. URL http://stacks.iop.org/0029-5515/50/i=12/a=125010.

[10] Y. Peysson, J. Decker, and L. Morini. A versatile ray-tracing code for studying rf wave propagation in toroidal magnetized plasmas. *Plasma Phys. Control. Fusion*, 54:045003, 2012.

[11] Y. Peysson and J. Decker. Calculation of rf current drive in tokamaks. CEA/IRFM, Association Euratom-CEA, 2007.

[12] Y. Peysson and J. Decker. Fast electron bremsstrahlung in axisymmetric magnetic configuration. *Physics of Plasmas*, 15, 2008.

[13] D. van Houtte et al. Recent fully non-inductive operation results in tore supra with 6 min, 1 gj plasma discharges. *Nuclear Fusion*, 44(5):L11, 2004.

[14] T. Mutoh et al. Steady-state operation and high energy particle production of mev energy in the large helical device. *Nuclear Fusion*, 47(9):1250, 2007. URL `http://stacks.iop.org/0029-5515/47/i=9/a=023`.

[15] Bibet. Conceptual study of a reflector waveguide array for launching lower hybrid waves in reactor grade plasmas. *Nuclear Fusion*.

[16] Ph. Bibet et al. Toward a lhcd system for iter. *Fusion Engineering and Design*, 74:419 – 423, 2005. ISSN 0920-3796. doi: 10.1016/j.fusengdes.2005.06.014. URL `http://www.sciencedirect.com/science/article/pii/S0920379605000840`. <ce:title>Proceedings of the 23rd Symposium of Fusion Technology</ce:title> <ce:subtitle>SOFT 23</ce:subtitle>.

[17] D. Guilhem et al. Manufacturing process and tests of a lower hybrid passive-active multijunction launcher for long pulse experiments on tore supra. *Fusion Engineering and Design*, 86(4-5):279–287, 2011.

[18] A. Ekedahl et al. Lower hybrid current drive in tore supra. *Fusion Science and Technology*, 56:1150–1172, 2009.

[19] M. Preynas, A. Ekedahl, N. Fedorczak, M. Goniche, D. Guilhem, J.P. Gunn, J. Hillairet, X. Litaudon, J. Achard, G. Berger-By, J. Belo, E. Corbel, L. Delpech, T. Ohsako, and M. Prou. Coupling characteristics of the iter-relevant lower hybrid antenna in tore supra: experiments and modelling. *Nuclear Fusion*, 51(2):023001, 2011. URL `http://stacks.iop.org/0029-5515/51/i=2/a=023001`.

[20] C. Gil. Diagnostic systems on tore supra. *Fusion Science and Technology*, (56): 1219–1252, 2009.

[21] J. Decker, Y. Peysson, J. Hillairet, J.-F. Artaud, V. Basiuk, A. Becoulet, A. Ekedahl, M. Goniche, G.T. Hoang, F. Imbeaux, A.K. Ram, and M. Schneider. Calculations of lower hybrid current drive in iter. *Nuclear Fusion*, 51(7):073025, 2011. URL `http://stacks.iop.org/0029-5515/51/i=7/a=073025`.

[22] K. Matsuda. Ray tracing study of the electron cyclotron current drive in diii-d using 60 ghz. *IEEE Transaction on plasma science*, 17(1):6–11, 1989.

A

Appendix

For each discharge mentioned in this work, I present some of the crucial plasma parameters in Table A.1, used as simulation input. Edge density at the mouth of the LH launcher, used as an input parameter in ALOHA, are taken from the Langmuir probe density measurement, from the Tore Supra database. The main parallel refractive index of the incident wave is calculated with ALOHA from phasing measurements from the Tore Supra database, after the agreement between aimed and actual phase difference between the modules is checked. Net LH power is obtained from the TS database. Central density, temperature, toroidal magnetic field at the center and loop voltage at the plasma edge is obtained from METIS output.

Table A.1: Crucial input parameters used in LHCD calculations for each scenario.

Discharge	LH power[MW]	$n_{e0}\,[\mathrm{m}^{-3}]$	$n_{edge}\,[\mathrm{m}^{-3}]$	$T_{e0}\,[\mathrm{keV}]$	$B\,[\mathrm{T}]$	main peak $n_{\parallel}$	$V_{loop}\,[\mathrm{mV}]$
#31527	1.95(C3)	$2.1 \cdot 10^{19}$	$4 \cdot 10^{17}$	4.1	3.4	1.72	0
#31528	0.85(C2) & 1.20(C3)	$2.0 \cdot 10^{19}$	$4 \cdot 10^{17}$	3.8	3.4	1.72 (C2) 1.72 (C3)	0
#32299	0.80(C2) & 2.10(C3)	$2.4 \cdot 10^{19}$	$5 \cdot 10^{17}$	4.6	3.4	1.67(C2) 1.72(C3)	0
#45525	2.10,2.60 (C4)	$1.4 \cdot 10^{19}$	$3 \cdot 10^{17}$	3.7	2.8	1.72, 1.81	0
#47955	3.00(C3) & 2.40(C4)	$4.0 \cdot 10^{19}$	$3 \cdot 10^{17}$	5.7	3.7	1.91 (C3) 1.72 (C4)	0
#47957	3.00(C3) & 2.40(C4)	$4.0 \cdot 10^{19}$	$3 \cdot 10^{17}$	5.7	3.7	1.91 (C3) 1.72 (C4)	0